

A Phenomenological Study of Semileptonic B^+ and B_s^0 Decays into Axial-Vector Mesons ($D_1(2420)$, $D_1'(2430)$, $D_{s1}(2460)$, and $D_{s1}'(2536)$) within the Standard Model

Rana Khan,¹ Qazi Maaz Us Salam,^{1,2,*} Zohaib Aarfi,³ and Ishtiaq Ahmed¹

¹*National Centre for Physics, Quaid-i-Azam University Campus, 45320, Islamabad, Pakistan*

²*Department of Physics, Lahore University of Management Sciences (LUMS),
Opposite Sector U, D.H.A, Lahore 54792, Pakistan*

³*Department of Physics and Astronomy, School of Natural Sciences,
National University of Sciences and Technology, H-12, Islamabad 44000, Pakistan*

Abstract

We study semileptonic B meson decays $B^+ \rightarrow D_1^{(\prime)} \ell^+ \nu_\ell$ and $B_s^0 \rightarrow D_{s1}^{-(\prime)} \ell^+ \nu_\ell$, where $\ell = \mu, \tau$. The final state axial vector mesons are treated as mixtures of the heavy quark basis states with light degree of freedom angular momenta $j_\ell = 1/2$ and $j_\ell = 3/2$, parametrized by the mixing angle θ_{D_1} . Using form factors obtained in the covariant light front quark model, we analyze the dependence of various observables on θ_{D_1} such as polarized and unpolarized branching ratios, the lepton forward-backward asymmetry, the longitudinal polarization fraction, and the lepton flavor universality ratios. In addition, we also discuss correlations among different observables. We study these observables in the experimentally motivated mixing angle regions as well as over a wider range of θ_{D_1} . Our results show that branching ratios and other observables are sensitive to the axial-vector mixing structure. These predictions provide useful Standard Model benchmarks for future measurements of semileptonic $B_{(s)}$ decays into orbitally excited mesons and may help to clarify the long standing $1/2$ vs. $3/2$ puzzle in semileptonic B decays.

arXiv:2605.12065v1 [hep-ph] 12 May 2026

* qazimaaz92@gmail.com

I. INTRODUCTION

The study of meson decays is one of the tools to test the theoretical framework of the Standard Model (SM) and to probe the internal structure of hadrons. In this context, semileptonic $B_{(s)} \rightarrow D_{(s)J}$ transitions have attracted considerable attention in recent decades, as they provide a clean environment to study heavy-quark dynamics and the properties of orbitally excited charm mesons [1–11]. Here $D_{(s)J}$ denotes both nonstrange and strange charmed mesons: D_J represents states with light-quark content $c\bar{q}$ ($q = u, d$), whereas D_{sJ} represents the corresponding strange states with $c\bar{s}$ content. The lowest s -wave states include the pseudoscalar and vector mesons, while the p -wave multiplet contains the scalar, axial-vector, and tensor states. In the present work, we focus on the axial-vector p -wave states $D_1(2420)$, $D'_1(2430)$, $D_{s1}(2460)$, and $D'_{s1}(2536)$.

They are classified using the spectroscopic $(^{2S+1})L_J$ notation. The scalar mesons $D_0^*(2300)$ and $D_{s0}^*(2317)$, which have quantum numbers $J^P = 0^+$, correspond to the 3P_0 state, while the axial-vector mesons with $J^P = 1^+$ arise from the two basis states 1P_1 and 3P_1 . In the heavy-quark limit, these states can also be classified using the $P_J^{j_\ell}$ notation,¹ for the axial-vector states, finite charm-quark-mass effects induce mixing between the $j_\ell = 1/2$ and $j_\ell = 3/2$ basis states. Therefore, the physical states are not pure j_ℓ eigenstates. They are commonly identified according to their dominant components: $D_1(2430)$ and $D_{s1}(2460)$ are mainly $j_\ell = 1/2$ states, whereas $D_1(2420)$ and $D_{s1}(2536)$ are mainly $j_\ell = 3/2$ states.

In the current study, we investigate the decays corresponding to $D_1(2420) \equiv D_1$, $D'_1(2430) \equiv D'_1$, $D_{s1}(2460) \equiv D_{s1}$, and $D_{s1}(2536) \equiv D'_{s1}$. The physical axial-vector states are obtained from the mixing of the $j_\ell = 1/2$ and $j_\ell = 3/2$ basis states, denoted by $|D_1^{1/2}\rangle$ and $|D_1^{3/2}\rangle$, respectively. This mixing can be parameterized in terms of a single mixing angle θ_{D_1} [12]

$$|D_{(s)1}\rangle = |D_1^{1/2}\rangle \sin \theta_{D_1} + |D_1^{3/2}\rangle \cos \theta_{D_1}, \quad (1)$$

$$|D'_{(s)1}\rangle = -|D_1^{3/2}\rangle \sin \theta_{D_1} + |D_1^{1/2}\rangle \cos \theta_{D_1}. \quad (2)$$

In the literature, as reported in [13], the analysis of the mixing angle θ_{D_1} was performed in the range $-45^\circ \leq \theta_{D_1} \leq -10^\circ$. It was further noted that the experimentally favored window for the decays $B \rightarrow (D_1, D'_1)\ell\nu_\ell$ lies within $-30.3^\circ \leq \theta_{D_1} \leq -24.9^\circ$. Motivated by this constraint, we first restrict our study to this experimentally preferred region in order to evaluate and analyze the relevant observables for the decays $B_s^0 \rightarrow (D_1^-, D_1'^-)\ell^+\nu_\ell$. In addition, we extend our analysis to the second experimentally allowed mixing-angle window, $43.3^\circ \leq \theta_{D_1} \leq 49.9^\circ$. We also perform a wider scan over the mixing angle, which provides an alternative allowed region corresponding to the same physical classification of the two axial-vector mesons.

It is worth noting that several puzzles exist in the spectroscopy of excited p -wave charmed mesons, including the $SU(3)$ mass-hierarchy problem and the low-mass puzzle associated mainly with the $D_0^*(2300)$, $D_{s0}^*(2317)$, and $D_{s1}(2460)$ states, as discussed in Refs. [14–17]. Another related issue is the long-standing so-called “1/2 vs. 3/2” puzzle in semileptonic B decays [18–22]. The so-called “1/2 vs. 3/2” puzzle refers to the tension between the heavy-quark-limit expectation and the observed pattern of semileptonic B decays into orbitally excited charmed mesons. In the heavy-quark limit, transitions to the broad $j_\ell = 1/2$ states are expected to be suppressed relative to those into the narrow $j_\ell = 3/2$ states. However, experimental measurements indicate that the rates into the $j_\ell = 1/2$ sector are not as small as expected, leading to a discrepancy between theoretical predictions and observed branching fractions [16, 17, 23]. This tension between theoretical predictions and experimental measurements has motivated various interpretations of the internal structure of these states, including compact tetra-quark configurations, hadronic molecular states, and possible mixing between conventional $c\bar{s}$ mesons and four-quark components, among other scenarios discussed in the refs [24–39].

From a theoretical perspective, semileptonic $B_{(s)}$ decays to the excited charmed mesons $D_0(2300)$, $D_{s0}(2317)$, $D_1(2420)$, $D'_1(2430)$, $D_{s1}(2460)$, and $D'_{s1}(2536)$ have been extensively studied using various approaches, including

¹ Here j_ℓ denotes the total angular momentum of the light degrees of freedom. For p -wave charmed mesons, the $j_\ell = 1/2$ doublet contains the $J^P = (0^+, 1^+)$ states, while the $j_\ell = 3/2$ doublet contains the $J^P = (1^+, 2^+)$ states.

the covariant light-front quark model (CLFQM) [5, 13, 40–45], the Isgur–Scora–Grinstein–Wise (ISGW) model [46], QCD sum rules [47–49], light-cone sum rules (LCSRs) [50], and heavy quark effective theory (HQET) [51–54]. In the present work, we employ hadronic form factors calculated within the CLFQM framework [13] to study semileptonic $b \rightarrow c$ transitions. Using these inputs, we analyze a range of physical observables for both polarized and unpolarized final-state mesons and investigate the impact of meson polarization on the full decay distributions.

In addition, a major motivation for studying flavor-changing charged-current (FCCC) processes such as $b \rightarrow c\ell\bar{\nu}$ in the B -meson sector is the presence of persistent tensions between experimental measurements and SM predictions. These discrepancies, typically at the level of 2σ – 4σ , are primarily observed in observables such as $R(D^{(*)})$, $R(J/\psi)$, and τ -polarization asymmetries [55–67], which provide important probes of possible new physics (NP) effects. To address these anomalies, several studies beyond the SM in the $b \rightarrow c$ sector have been performed in recent years [68–77]. In this context, we also study different lepton flavor universality (LFU) ratios as a complementary analysis.

In this work, we present a phenomenological analysis of the semileptonic decays $B^+ \rightarrow D_1^{(\prime)}\ell^+\nu_\ell$ and $B_s^0 \rightarrow D_{s1}^{-(\prime)}\ell^+\nu_\ell$, where $\ell = \mu, \tau$. We study several physical observables, including the branching ratios and lepton forward-backward asymmetry \mathcal{A}_{FB} with the longitudinal and transverse polarization of the final-state meson, the longitudinal polarization fraction F_L and lepton flavor universality ratio $\mathcal{R}_{D_1^{(\prime)}}$ and $\mathcal{R}_{D_{s1}^{(\prime)}}$. Keeping in view the experimental data of the branching ratio for $B^+ \rightarrow D_1, D_1'$, it is expected that in future the results of other decay distributions and different angular observables will be available with much better statistics. Therefore, in addition to the branching ratio calculation, we have studied the impact of other polarized and unpolarized observables over the parameter θ_{D_1} in wide range of angle.

The rest of the paper is organized as follows. In Sec. II, we present the theoretical framework and define the relevant observables used in our analysis. In Sec. III, we carry out a comprehensive phenomenological study. In particular, in Sec. III A, we examine the dependence of various observables on the mixing angle. The q^2 -dependent behavior of these observables are analyzed in Sec. III B. Furthermore, in Sec. III C, we provide the correlations among different observables. Finally, in Sec. IV, we conclude our work and give the supporting details in the appendices.

II. THEORETICAL FRAMEWORK

At the quark level, the semileptonic transition $b \rightarrow c\bar{\ell}\nu_\ell$ is governed by the weak effective Hamiltonian given as follows,

$$\mathcal{H}_{\text{eff}}^{b \rightarrow c} = \frac{G_F}{\sqrt{2}} V_{cb} (\bar{c}\gamma_\mu P_L b) (\bar{\ell}\gamma_\mu P_L \nu_\ell) \quad (3)$$

Where $P_L = (1 - \gamma_5)/2$, G_F is the Fermi constant, and V_{cb} is the relevant CKM matrix element. It is established that the physical states $D_{(s)1}^{(\prime)} = \{D_1, D_1', D_{s1}, D_{s1}'\}$ are mixtures of $D_1^{3/2}$ and $D_1^{1/2}$ such as defined in Eq. (1) and Eq. (2). Consequently, the hadronic transition between the initial B^+ and $B_{(s)}$ meson and the final axial vector meson $D_1^{(\prime)}$ and $D_{s1}^{(\prime)}$ can be expressed in terms of these mixed states. Furthermore, we can write these Hadronic matrix element (HMEs) in the weak eigenstate basis as,

$$\begin{aligned} \langle {}^i D_1(k) | \gamma^\mu | B_{(s)}^{0,+}(p) \rangle = & -i \left[(m_{B_{(s)}^{0,+}} - m_{i D_1}) \varepsilon^{\mu*} V_1^{i D_1}(q^2) - \frac{\varepsilon^* \cdot P}{m_{B_{(s)}^{0,+}} - m_{i D_1}} P_\mu V_2^{i D_1}(q^2) \right. \\ & \left. - 2m_{i D_1} \frac{\varepsilon^* \cdot P}{q^2} q^\mu \left(V_3^{i D_1}(q^2) - V_0^{i D_1}(q^2) \right) \right], \end{aligned} \quad (4)$$

$$\langle {}^i D_1(k) | \gamma^\mu \gamma^5 | B_{(s)}^{0,+}(p) \rangle = - \frac{1}{m_{B_{(s)}^{0,+}} - m_{i D_1}} \varepsilon^{\mu\nu\alpha\beta} \varepsilon^{\nu*} P^\alpha q^\beta A^{i D_1}(q^2), \quad (5)$$

Here $p(k)$ denotes the four momentum of the initial (final) meson and q^2 is the square of the momentum transfer. Whereas, $P = p + k$, $q = p - k$, and the conventions $\epsilon^{0123} = 1$ is adopted. The superscript i labels the weak eigenstates, with $i = 1/2$ and $3/2$. Accordingly, the states are denoted as $D_1^{1/2}$ and $D_1^{3/2}$. The scalar functions

$A_0(q^2)$, $V_0(q^2)$, $V_1(q^2)$, and $V_2(q^2)$ are the hadronic form factors (FFs) defined in Eq. (14), which constitute the primary source of hadronic uncertainties and computed within the CLFQM, as reported in [13].

In order to calculate the decay amplitude from the effective Hamiltonian given in Eq. (3), the physical states D_1 , D_{s1} , D'_1 and D'_{s1} will appear. These states are obtained from the weak eigenstates $D_1^{1/2}$ and $D_1^{3/2}$ through the mixing relations given in Eqs. (1) and (2).

A. PHYSICAL OBSERVABLE

In order to compute the decay observables, we start from the transition amplitude derived from the effective Hamiltonian $\mathcal{H}_{\text{eff}}^{b \rightarrow c}$ given in Eq. (3). Taking into account the two-body phase space, the hadronic matrix elements (HMEs) that are evaluated using the scalar products of the relevant four-momenta and the kinematic relations summarized in Appendix A–C. The analysis is performed separately for the polarized and unpolarized cases. Using the HMEs defined in Eqs. (4) and (5), along with the necessary scalar products listed in Appendix A–C, we obtain the final two-fold differential decay rate for the processes $B^+ \rightarrow D_1^{(\prime)} \ell^+ \nu_\ell$ and $B_s^0 \rightarrow D_{s1}^{-(\prime)} \ell^+ \nu_\ell$, where $\ell = \mu, \tau$ with an unpolarized final state mesons $D_1^{(\prime)}$ and $D_{s1}^{(\prime)}$ as,

$$\begin{aligned} \frac{d\Gamma}{dq^2} = & \frac{G_F^2 |V_{cb}|^2 q^2}{192\pi^3 2m_{B_{(s)}}^3} \sqrt{\lambda(m_{B_{(s)}}^2, m_{D_{(s)1}^{(\prime)}}^2, q^2)} \left(1 - \frac{m_\ell^2}{q^2}\right)^2 \times \\ & \left\{ (m_\ell^2 + 2q^2) \left| \frac{1}{2m_{D_{(s)1}^{(\prime)}}} \left[(m_{B_{(s)}}^2 - m_{D_{(s)1}^{(\prime)}}^2 - q^2)(m_{B_{(s)}} - m_{D_{(s)1}^{(\prime)}}) V_1(q^2) - \frac{\lambda(m_{B_{(s)}}^2, m_{D_{(s)1}^{(\prime)}}^2, q^2)}{m_{B_{(s)}} - m_{D_{(s)1}^{(\prime)}}} V_2(q^2) \right] \right|^2 \right. \\ & (m_\ell^2 + 2q^2) \lambda(m_{B_{(s)}}^2, m_{D_{(s)1}^{(\prime)}}^2, q^2) \left| \frac{A_0(q^2)}{m_{B_{(s)}} - m_{D_{(s)1}^{(\prime)}}} \mp \frac{(m_{B_{(s)}} - m_{D_{(s)1}^{(\prime)}}) V_1(q^2)}{\sqrt{\lambda(m_{B_{(s)}}^2, m_{D_{(s)1}^{(\prime)}}^2, q^2)}} \right|^2 \\ & \left. + 3m_\ell^2 \lambda(m_{B_{(s)}}^2, m_{D_{(s)1}^{(\prime)}}^2, q^2) V_0^2(q^2) \right\} \end{aligned} \quad (6)$$

Where $\lambda(m_{B_{(s)}}^2, m_{D_{(s)1}^{(\prime)}}^2, q^2) = (m_{B_{(s)}}^2 + m_{D_{(s)1}^{(\prime)}}^2 + q^2)^2 - 4m_{B_{(s)}}^2 m_{D_{(s)1}^{(\prime)}}^2$ is the Kallen function, and m_ℓ denotes the mass of the charged lepton with $\ell = \mu, \tau$.

For the case of longitudinal and transverse final state meson polarization, L and T polarized two-fold angular decay distribution is,

$$\begin{aligned} \frac{d\Gamma_L}{dq^2} = & \frac{G_F^2 |V_{cb}|^2 q^2}{192\pi^3 2m_{B_{(s)}}^3} \sqrt{\lambda(m_{B_{(s)}}^2, m_{D_{(s)1}^{(\prime)}}^2, q^2)} \left(1 - \frac{m_\ell^2}{q^2}\right)^2 \times \\ & \left\{ 3m_\ell^2 \lambda(m_{B_{(s)}}^2, m_{D_{(s)1}^{(\prime)}}^2, q^2) V_0^2(q^2) + (m_\ell^2 + 2q^2) \right. \\ & \left. \times \left| \frac{1}{2m_{D_{(s)1}^{(\prime)}}} \left[(m_{B_{(s)}}^2 - m_{D_{(s)1}^{(\prime)}}^2 - q^2)(m_{B_{(s)}} - m_{D_{(s)1}^{(\prime)}}) V_1(q^2) - \frac{\lambda(m_{B_{(s)}}^2, m_{D_{(s)1}^{(\prime)}}^2, q^2)}{m_{B_{(s)}} - m_{D_{(s)1}^{(\prime)}}} V_2(q^2) \right] \right|^2 \right\} \end{aligned} \quad (7)$$

$$\begin{aligned} \frac{d\Gamma_\pm}{dq^2} = & \frac{G_F^2 |V_{cb}|^2 q^2}{192\pi^3 2m_{B_{(s)}}^3} \sqrt{\lambda(m_{B_{(s)}}^2, m_{D_{(s)1}^{(\prime)}}^2, q^2)} \left(1 - \frac{m_\ell^2}{q^2}\right)^2 \times \\ & \left\{ (m_\ell^2 + 2q^2) \lambda(m_{B_{(s)}}^2, m_{D_{(s)1}^{(\prime)}}^2, q^2) \left| \frac{A_0(q^2)}{m_{B_{(s)}} - m_{D_{(s)1}^{(\prime)}}} \mp \frac{(m_{B_{(s)}} - m_{D_{(s)1}^{(\prime)}}) V_1(q^2)}{\sqrt{\lambda(m_{B_{(s)}}^2, m_{D_{(s)1}^{(\prime)}}^2, q^2)}} \right|^2 \right\} \end{aligned} \quad (8)$$

- The polarized and unpolarized differential branching ratio are related to the decay rate as follow,

$$\frac{d^2\mathcal{B}}{dq^2} = \tau_{B_{(s)}^{0,+}} \frac{d^2\Gamma}{dq^2}, \quad \frac{d^2\mathcal{B}_L}{dq^2} = \tau_{B_{(s)}^{0,+}} \frac{d^2\Gamma_L}{dq^2}, \quad \frac{d^2\mathcal{B}_T}{dq^2} = \tau_{B_{(s)}^{0,+}} \left(\frac{d^2\Gamma_+}{dq^2} + \frac{d^2\Gamma_-}{dq^2} \right), \quad (9)$$

where $\tau_{B_{(s)}^{0,+}}$ is the lifetime of the initial meson B_s^0 and B^+ .

- For the decay the lepton forward backward asymmetry is defined with respect to the angle θ , which denotes the angle between the three momentum of the charged lepton and that of the final state meson in the dilepton center of mass frame. It is given by,

$$\mathcal{A}_{\text{FB}}(q^2) = \frac{\int_0^1 \frac{d^2\Gamma}{dq^2 d\cos\theta} d\cos\theta - \int_{-1}^0 \frac{d^2\Gamma}{dq^2 d\cos\theta} d\cos\theta}{\int_{-1}^1 \frac{d^2\Gamma}{dq^2 d\cos\theta} d\cos\theta}. \quad (10)$$

- The longitudinal polarization fraction $F_L(q^2)$ as a function of the momentum transfer is defined as

$$F_L(q^2) = \frac{\int_{-1}^1 \frac{d^2\Gamma_L}{dq^2 d\cos\theta} d\cos\theta}{\int_{-1}^1 \frac{d^2\Gamma}{dq^2 d\cos\theta} d\cos\theta}, \quad (11)$$

where Γ_L denotes the partial decay width corresponding to the longitudinal polarization of the final state meson.

- We also constructed the ratio of branching fraction to muon generation. In the present context for the $B^+ \rightarrow D_1^{(\prime)} \ell^+ \nu_\ell$ and $B_s^0 \rightarrow D_{s1}^{-(\prime)} \ell^+ \nu_\ell$, we define the ratio $\mathcal{R}_{D_1^{(\prime)}}$ and $\mathcal{R}_{D_{s1}^{(\prime)}}$ as,

$$\mathcal{R}_{D_1^{(\prime)}}(q^2) = \frac{\int_{q_{\min}^2}^{q_{\max}^2} \frac{d\mathcal{B}(B^+ \rightarrow D_1^{(\prime)} \tau \nu)}{dq^2} dq^2}{\int_{q_{\min}^2}^{q_{\max}^2} \frac{d\mathcal{B}(B^+ \rightarrow D_1^{(\prime)} \mu \nu)}{dq^2} dq^2} \quad \mathcal{R}_{D_{s1}^{(\prime)}}(q^2) = \frac{\int_{q_{\min}^2}^{q_{\max}^2} \frac{d\mathcal{B}(B_s^0 \rightarrow D_{s1}^{-(\prime)} \tau \nu)}{dq^2} dq^2}{\int_{q_{\min}^2}^{q_{\max}^2} \frac{d\mathcal{B}(B_s^0 \rightarrow D_{s1}^{-(\prime)} \mu \nu)}{dq^2} dq^2} \quad (12)$$

where the integration is over the appropriate q^2 bins for comparison with the experimental data.

- We also constructed polarized branching ratio and lepton forward asymmetry for the decay. The combined transverse and total differential decay widths are defined as

$$\frac{d\Gamma}{dq^2} = \frac{d\Gamma_L}{dq^2} + \frac{d\Gamma_T}{dq^2}, \quad \frac{d\Gamma_T}{dq^2} = \frac{d\Gamma_+}{dq^2} + \frac{d\Gamma_-}{dq^2}. \quad (13)$$

The Γ_+ and Γ_- represent the contributions from the two transverse helicity states [13].

- For the longitudinally (L) and transversely (T) polarized cases, the lepton forward backward asymmetry is defined using the same expression as in Eq. (10), with the unpolarized decay rate replaced by the corresponding polarized decay rates Γ_L and Γ_T , respectively.

III. PHENOMENOLOGICAL ANALYSIS

In this section, we analyze the physical observables introduced in Section II A within the framework of the SM. To do so, the input parameters taken from [78] relevant to our analysis are given in the TABLE. I.

The hadronization of quarks and gluons is described in terms of transition FFs constitute the dominant source of theoretical uncertainties. In our numerical analysis, the FFs that we use for $B^+ \rightarrow D_1^{(\prime)} \ell^+ \nu_\ell$ and $B_s^0 \rightarrow D_{s1}^{-(\prime)} \ell^+ \nu_\ell$,

TABLE I: The values of the input parameters [78].

Constant	Value	Constant	Value	Constant	Value
m_b	4.183 GeV	m_{D_1}	2.420 GeV	τ_{B^+}	1.638×10^{-12} s
m_μ	0.106 GeV	m_{B^+}	5.279 GeV	V_{cb}	40.3×10^{-3}
m_u	0.003 GeV	$m_{D'_1}$	2.430 GeV	$\tau_{B_s^0}$	1.520×10^{-12} s
m_s	0.093 GeV	$m_{D_{s1}}$	2.460 GeV	$m_{D'_{s1}}$	2.536 GeV
m_τ	1.77 GeV	$m_{B_s^0}$	5.367 GeV	G_F	1.166×10^{-5} GeV $^{-2}$

where $\ell = \mu, \tau$ are calculated within the CLFQM, as reported in [13]. These form factors are extrapolated using a double pole parametrization of the form,

$$F(q^2) = \frac{F(0)}{1 + a \left(\frac{q^2}{m_{B_{(s)}^{0,+}}^2} \right) - b \left(\frac{q^2}{m_{B_{(s)}^{0,+}}^2} \right)^2}, \quad (14)$$

where $m_{B_{(s)}^{0,+}}$ denotes the masses of the initial $B_{(s)}^{0,+}$ mesons and $F(q^2)$ represents the relevant transition FFs, namely $A_0^{D_{(s)1}^{(\prime)}}$, $V_0^{D_{(s)1}^{(\prime)}}$, $V_1^{D_{(s)1}^{(\prime)}}$ and $V_2^{D_{(s)1}^{(\prime)}}$ given in TABLE II.

TABLE II: The form factors of the transitions $B^+ \rightarrow D_1^{(\prime)\ell^+\nu_\ell}$ and $B_s^0 \rightarrow D_{s1}^{-(\prime)\ell^+\nu_\ell}$, in the covariant light-front quark model [13].

FFs	$F(0)$	a	b	FFs	$F(0)$	a	b
$A_0^{D_1}$	$+0.20^{+0.022}_{-0.022}$	$-0.27^{+0.802}_{-0.114}$	$+0.11^{+0.028}_{-0.036}$	$A_0^{D_{s1}}$	$+0.20^{+0.023}_{-0.021}$	$-0.27^{+0.801}_{-0.114}$	$+0.11^{+0.020}_{-0.031}$
$V_0^{D_1}$	$+0.40^{+0.044}_{-0.044}$	$-0.17^{+0.044}_{-0.072}$	$-0.02^{+0.010}_{-0.010}$	$V_0^{D_{s1}}$	$+0.40^{+0.041}_{-0.042}$	$-0.17^{+0.041}_{-0.073}$	$-0.02^{+0.012}_{-0.013}$
$V_1^{D_1}$	$+0.58^{+0.031}_{-0.044}$	$-0.05^{+0.014}_{-0.014}$	$+0.02^{+0.010}_{-0.000}$	$V_1^{D_{s1}}$	$+0.58^{+0.033}_{-0.041}$	$-0.05^{+0.01}_{-0.013}$	$+0.02^{+0.011}_{+0.000}$
$V_2^{D_1}$	$-0.05^{+0.022}_{-0.010}$	$+0.56^{+0.228}_{-0.257}$	$+2.50^{+1.688}_{-1.315}$	$V_2^{D_{s1}}$	$-0.05^{+0.021}_{-0.011}$	$+0.56^{+0.223}_{-0.252}$	$+2.50^{+1.682}_{-1.311}$
$A_0^{D'_1}$	$+0.08^{+0.022}_{-0.022}$	$+2.05^{+0.373}_{-0.350}$	$+5.57^{+0.559}_{-0.456}$	$A_0^{D'_{s1}}$	$+0.08^{+0.022}_{-0.021}$	$+2.05^{+0.372}_{-0.351}$	$+5.57^{+0.552}_{-0.451}$
$V_0^{D'_1}$	$-0.08^{+0.041}_{-0.041}$	$+1.24^{+0.235}_{-0.257}$	$+0.74^{+0.210}_{-0.171}$	$V_0^{D'_{s1}}$	$-0.08^{+0.043}_{-0.040}$	$+1.24^{+0.232}_{-0.252}$	$+0.74^{+0.213}_{-0.174}$
$V_1^{D'_1}$	$+0.17^{+0.044}_{-0.042}$	$-0.52^{+0.084}_{-0.078}$	$+0.36^{+0.031}_{-0.080}$	$V_1^{D'_{s1}}$	$+0.17^{+0.040}_{-0.042}$	$-0.52^{+0.081}_{-0.073}$	$+0.36^{+0.032}_{-0.081}$
$V_2^{D'_1}$	$+0.11^{+0.014}_{-0.028}$	$+0.25^{+0.084}_{-0.098}$	$-0.07^{+0.031}_{-0.050}$	$V_2^{D'_{s1}}$	$+0.11^{+0.011}_{-0.025}$	$+0.25^{+0.083}_{-0.090}$	$-0.07^{+0.033}_{-0.051}$

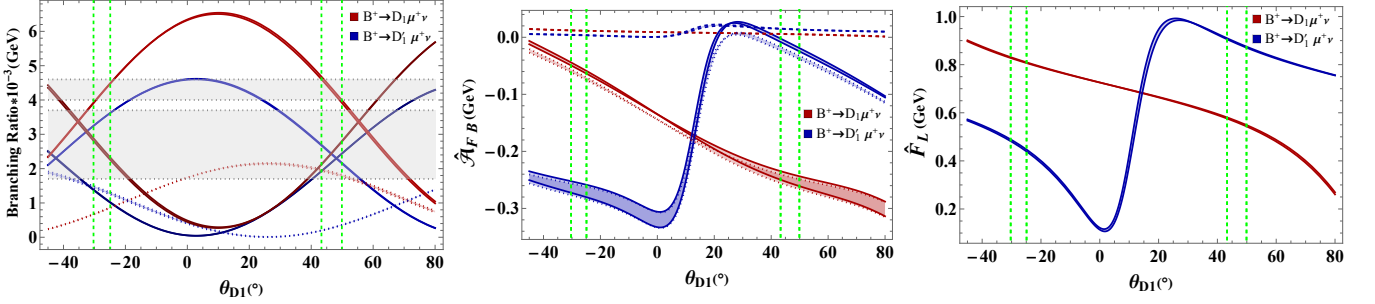
The uncertainties in the FFs parameters originate from both statistical and systematic sources and are quoted in quadrature. Since the covariance matrix among the fitted parameters is not available, correlations among $F(0)$, a , and b are neglected, and the total uncertainty of the FFs is estimated by standard Gaussian error propagation. In the next step, with these input parameters, the task is to perform the phenomenological analysis of the $B^+ \rightarrow D_1^{(\prime)\ell^+\nu_\ell}$ and $B_s^0 \rightarrow D_{s1}^{-(\prime)\ell^+\nu_\ell}$ decay, with $\ell = \mu, \tau$.

A. Mixing Angle Dependence of Observables in $B^+ \rightarrow D_1^{(\prime)\ell^+\nu_\ell}$ and $B_s^0 \rightarrow D_{s1}^{-(\prime)\ell^+\nu_\ell}$ decays

In FIG. 1 we present the differential branching ratios, \mathcal{A}_{FB} and F_L as functions of θ_{D_1} for the decay $B^+ \rightarrow D_1^{(\prime)\mu\nu\mu}$. As indicated by the legend in the plot, the darker red band corresponds to $B^+ \rightarrow D_1\mu\nu\mu$, while the darker blue band corresponds to $B^+ \rightarrow D_1'\mu\nu$. The solid line shows the unpolarized behavior, while the dashed (dotted) line shows the longitudinally (transversely) polarized final state meson, respectively. The bands in these plots originate from the errors in the input parameters, mainly the FFs. For the branching ratios, we present the experimentally accessible ranges, the upper (lower) shaded band corresponds to the decay channels $B^+ \rightarrow D_1\mu^+\nu$ ($B^+ \rightarrow D_1'\mu^+\nu$) respectively. The mixing angle is considered within two ranges shown in green vertical dashed lines, $\theta_{D_1} \in [-30.3^\circ, -24.9^\circ]$ and $\theta_{D_1} \in [43.3^\circ, 49.9^\circ]$. The obtained results lie within these ranges and are consistent within current experimental uncertainties with the currently available experimental data [78]. At present, experimental

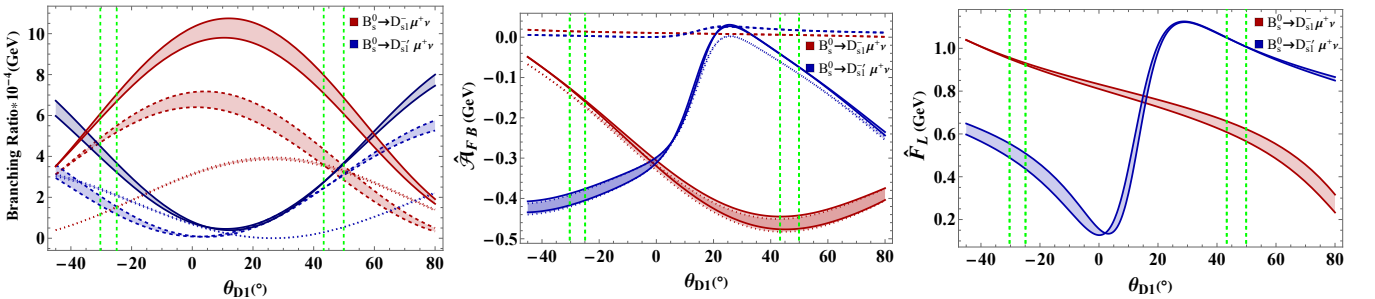
measurements are primarily limited to the branching ratios, which alone may not be sufficient to fully resolve the existing tension between theoretical predictions and experimental data. In this work, we have also provided predictions for additional observables \mathcal{A}_{FB} and F_L within the same angle ranges. Future measurements of these observables in the $B^+ \rightarrow D_1^{(\prime)} \ell^+ \nu_\ell$ and $B_s^0 \rightarrow D_{s1}^{-(\prime)} \ell^+ \nu_\ell$ channels could provide crucial complementary information and help clarify this tension that cannot be addressed by branching ratio measurements alone. From the plots, we can read as,

FIG. 1: The mixing angle θ_{D_1} dependencies of the polarized branching ratios, lepton forward backward asymmetry and longitudinal fraction for the semileptonic decays $B^+ \rightarrow D_1 \mu^+ \nu$ and $B^+ \rightarrow D_1' \mu^+ \nu$.



- The branching ratio of $B^+ \rightarrow D_1 \mu^+ \nu$ increases when θ_{D_1} lies in the negative range $[-30.3^\circ, -24.9^\circ]$ and decreases in the positive range $[43.3^\circ, 49.9^\circ]$. In contrast, the decay $B^+ \rightarrow D_1' \mu^+ \nu$ shows the opposite behavior. The L and T polarized observables follow the same behavior as the unpolarized case, but with smaller magnitudes. The L contribution is larger than the T one.
- For \mathcal{A}_{FB} , the T polarization component is found to be dominant for both D_1 and D_1' channels, while the L contribution remains close to zero over the full θ_{D_1} range. For the D_1 channel, within the negative mixing angle range $\theta_{D_1} \in [-30.3^\circ, -24.9^\circ]$, the forward-backward asymmetry varies as $[-0.257, -0.263]$, while in the positive range $\theta_{D_1} \in [43.3^\circ, 49.9^\circ]$, it takes values $[0.002, 0.019]$. For the D_1' channel in the negative (positive) θ_{D_1} range as mentioned before, the asymmetry lies within $[-0.056, -0.059]$ ($[0.250, 0.241]$), respectively.
- Similarly, for F_L , we obtain $[0.828, 0.810]$ for the D_1 state in the mentioned negative θ_{D_1} region and $[0.581, 0.543]$ in the positive θ_{D_1} region. For the D_1' channel, the corresponding ranges are given by $[0.489, 0.447]$ in the negative angle region and $[0.904, 0.873]$ in the positive angle region. Since no experimental data are currently available for these observables, future experiments can probe and measure their values.

FIG. 2: The mixing angle θ_{D_1} dependencies of the polarized branching ratios, lepton forward backward asymmetry and longitudinal fraction for the semileptonic decays $B_s^0 \rightarrow D_{s1}^- \mu^+ \nu_\ell$ and $B_s^0 \rightarrow D_{s1}'^- \mu^+ \nu_\ell$.



- In FIG. 2, the branching ratio of $B^+ \rightarrow D_{s1}\mu^+\nu$ increases in $\theta_{D1} \in [-30.3^\circ, -24.9^\circ]$ range, where it varies within $[0.610, 0.702] \times 10^{-3}$, and decreases in the range $\theta_{D1} \in [43.3^\circ, 49.9^\circ]$, taking values within $[0.799, 0.606] \times 10^{-3}$. In contrast, the decay $B^+ \rightarrow D'_{s1}\mu^+\nu$ shows the opposite behavior, with the branching ratio lying in the range $[0.456, 0.324] \times 10^{-3}$ for as mentioned negative θ_{D1} and $[0.247, 0.313] \times 10^{-3}$ for positive θ_{D1} . The L and T polarized observables follow the same trend as the unpolarized case, but with smaller magnitudes. The L contribution remains dominant over the T contribution across the full range of the mixing angle.
- For \mathcal{A}_{FB} , the T polarization component remains dominant for both D_{s1} and D'_{s1} channels, while the L contribution stays close to zero over the full θ_{D1} range. For the D_{s1} state, within the negative mixing angle range $\theta_{D1} \in [-30.3^\circ, -24.9^\circ]$, the forward-backward asymmetry varies as $[-0.411, -0.393]$, while in the positive range $\theta_{D1} \in [43.3^\circ, 49.9^\circ]$, it takes values $[-0.042, -0.091]$. For the D'_{s1} channel, with \mathcal{A}_{FB} spanning the ranges $[-0.128, -0.160]$ in the aforementioned negative angle region and $[-0.467, -0.458]$ in the positive angle region. The two channels show clearly different magnitudes across the given θ_{D1} range.
- Similarly, for F_L , shows a θ_{D1} dependence for both channels. For the D_{s1} state, we obtain $[0.951, 0.921]$ in the $\theta_{D1} \in [-30.3^\circ, -24.9^\circ]$ region and $[0.635, 0.594]$ in the $\theta_{D1} \in [43.3^\circ, 49.9^\circ]$ region. For the D'_{s1} channel, the corresponding ranges are shown in the plots.

In the absence of experimental data for these observables for $B^+ \rightarrow D_1^{(\prime)}\ell^+\nu_\ell$ and $B_s^0 \rightarrow D_{s1}^{-(\prime)}\ell^+\nu_\ell$ decays, our results may serve as theoretical predictions; furthermore, future experiments can test these predicted values. The different patterns seen for both D_{s1} and D'_{s1} in the negative and positive θ_{D1} region show that these physical observables, such as the branching ratio, \mathcal{A}_{FB} and F_L are highly sensitive to the mixing angle. This sensitivity can help us better understand the current tension between theoretical predictions and experimental results.

B. q^2 -dependent analysis of the Observables in the $B^+ \rightarrow D_1^{(\prime)}\ell^+\nu_\ell$ and $B_s^0 \rightarrow D_{s1}^{-(\prime)}\ell^+\nu_\ell$ decays.

In this section, we compute the branching ratios, \mathcal{A}_{FB} , and F_L as functions of the momentum transfer q^2 for the decay channels $B^+ \rightarrow D_1^{(\prime)}\ell^+\nu_\ell$ and $B_s^0 \rightarrow D_{s1}^{-(\prime)}\ell^+\nu_\ell$, where $\ell = \mu, \tau$. We also present the polarized branching ratio and lepton forward backward asymmetry for the cases where the final state meson is L or T polarized. The red curve corresponds to the unpolarized result, while the blue and purple curves represent the L and T polarization contributions, respectively, as shown in FIGs (3-10). The bands in these plots arise from the uncertainties in the input parameters, mainly the form factors, as well as from the maximum and minimum values of θ_{D1} , where $\theta_{D1} \in [-30.3^\circ, -24.9^\circ]$ and $\theta_{D1} \in [43.3^\circ, 49.9^\circ]$. It is important to emphasize that the spread associated with θ_{D1} does not represent a theoretical uncertainty, but instead, it arises from varying the mixing angle over its allowed range.

We present the bin-averaged values of the observables using a bin width of $\Delta q^2 = 1 \text{ GeV}^2$. The corresponding binned differential branching ratio is defined by,

$$\left\langle \frac{d\mathcal{B}}{dq^2} \right\rangle_{[q_{\min}^2, q_{\max}^2]} = \frac{\int_{q_{\min}^2}^{q_{\max}^2} \left(\frac{d\mathcal{B}}{dq^2} \right) dq^2}{q_{\max}^2 - q_{\min}^2}. \quad (15)$$

The binned lepton forward backward and longitudinal fraction are defined as,

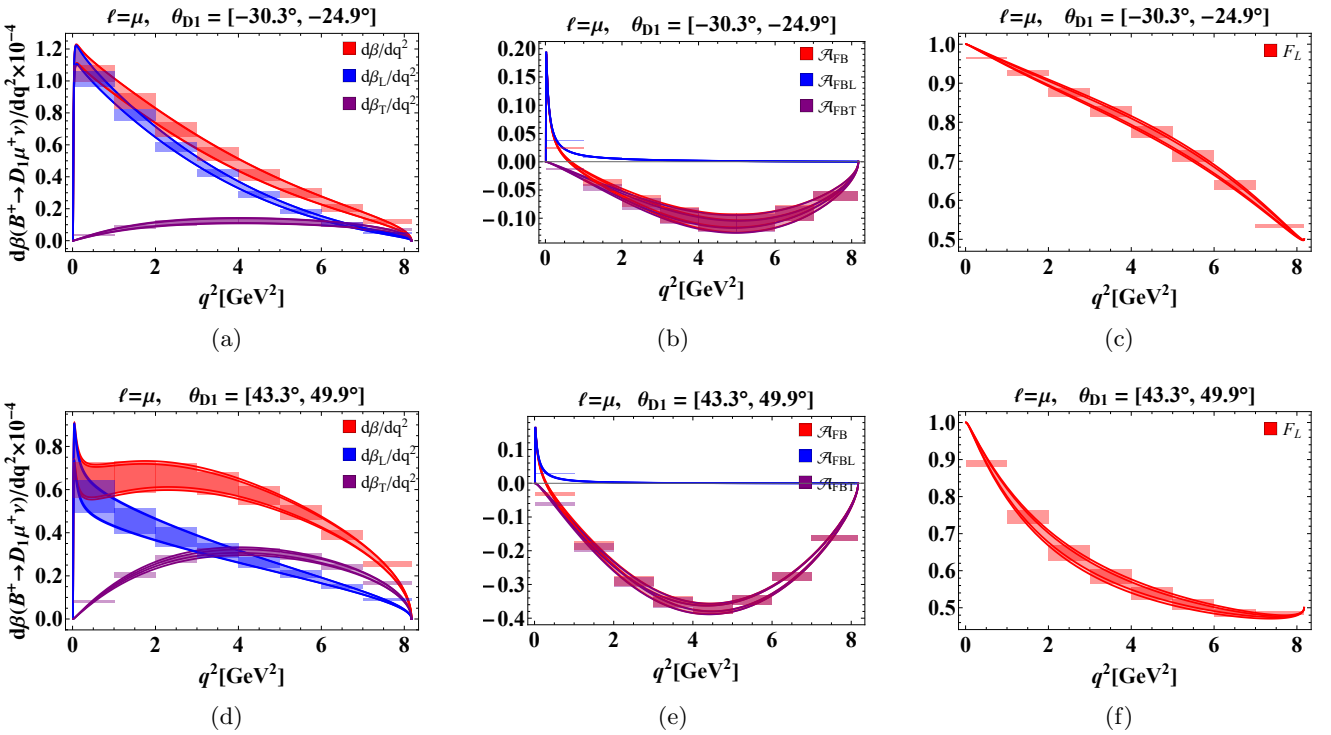
$$\langle F_L \rangle_{[q_{\min}^2, q_{\max}^2]} = \frac{\int_{q_{\min}^2}^{q_{\max}^2} F_L(q^2) \frac{d\Gamma}{dq^2} dq^2}{\int_{q_{\min}^2}^{q_{\max}^2} \frac{d\Gamma}{dq^2} dq^2}, \quad \langle \mathcal{A}_{FB} \rangle_{[q_{\min}^2, q_{\max}^2]} = \frac{\int_{q_{\min}^2}^{q_{\max}^2} \mathcal{A}_{FB}(q^2) \frac{d\Gamma}{dq^2} dq^2}{\int_{q_{\min}^2}^{q_{\max}^2} \frac{d\Gamma}{dq^2} dq^2}. \quad (16)$$

The binned analysis of the ratio $R_{D_1^{(\prime)}}$ and $R_{D_{s1}^{(\prime)}}$ is performed using the following definition,

$$\langle \mathcal{R}_{D_1^{(\prime)}} \rangle_{[q_{\min}^2, q_{\max}^2]} = \frac{\int_{q_{\min}^2}^{q_{\max}^2} \frac{d\mathcal{B}(B^+ \rightarrow D_1^{(\prime)} \tau^+ \nu_\tau)}{dq^2} dq^2}{\int_{q_{\min}^2}^{q_{\max}^2} \frac{d\mathcal{B}(B^+ \rightarrow D_1^{(\prime)} \mu^+ \nu_\mu)}{dq^2} dq^2}, \quad \langle \mathcal{R}_{D_{s1}^{(\prime)}} \rangle_{[q_{\min}^2, q_{\max}^2]} = \frac{\int_{q_{\min}^2}^{q_{\max}^2} \frac{d\mathcal{B}(B_s^0 \rightarrow D_{s1}^{-(\prime)} \tau^+ \nu_\tau)}{dq^2} dq^2}{\int_{q_{\min}^2}^{q_{\max}^2} \frac{d\mathcal{B}(B_s^0 \rightarrow D_{s1}^{-(\prime)} \mu^+ \nu_\mu)}{dq^2} dq^2} \quad (17)$$

1. Observable for the decay of $B^+ \rightarrow D_1 \ell^+ \nu_\ell$.

FIG. 3: The polarized and unpolarized branching ratio, lepton forward backward asymmetry, and the longitudinal fraction as a function of q^2 for $B^+ \rightarrow D_1 \mu^+ \nu$ transition.

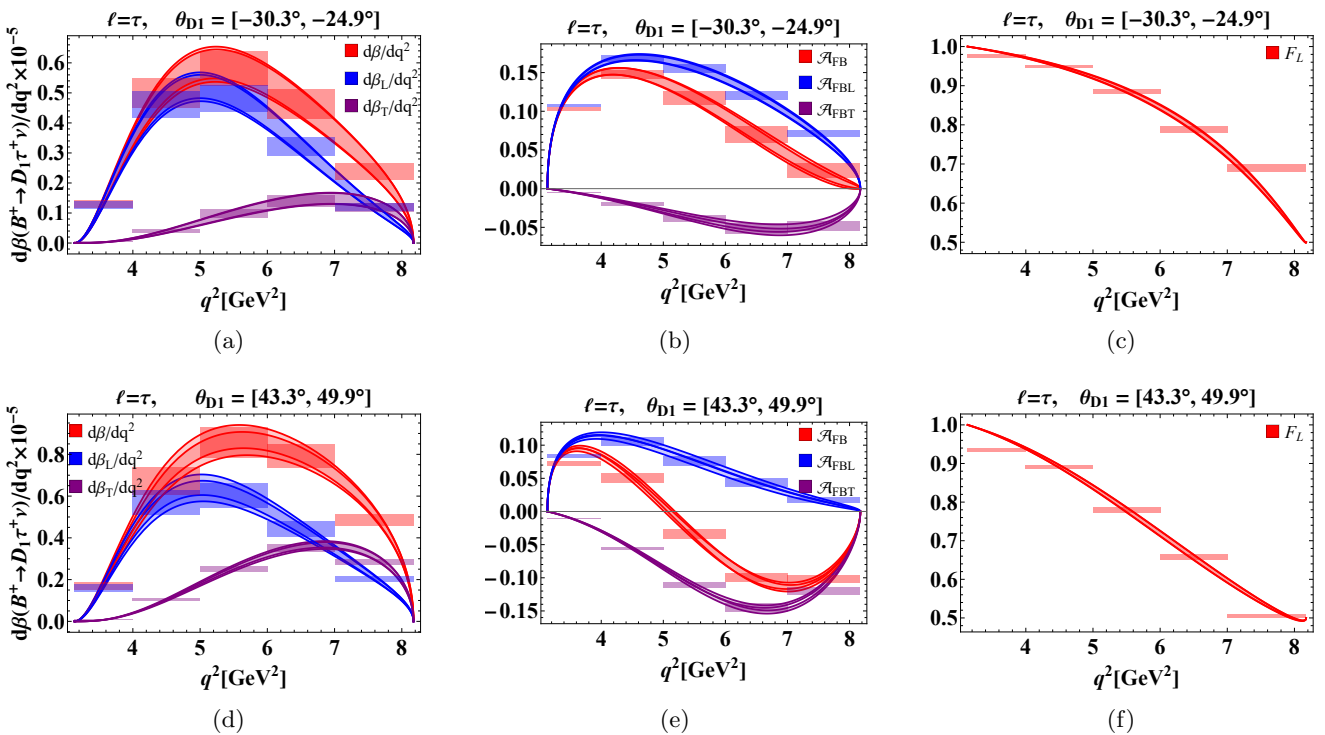


FIGS. 3 shows the polarized and unpolarized branching ratio, lepton forward-backward asymmetry, and longitudinal fraction as functions of q^2 for the $B^+ \rightarrow D_1 \mu^+ \nu$ transition. The first row corresponds to the fixed mixing-angle range $\theta_{D1} \in [-30.3^\circ, -24.9^\circ]$, while the second row corresponds to $\theta_{D1} \in [43.3^\circ, 49.9^\circ]$.

- FIG. 3a shows the differential branching ratio, including both the unpolarized result and the contributions from the polarized final state meson. As we observe, over the whole kinematic region, the L polarization contribution is dominant over the T one. The L and T contributions do not follow the same trend: over most of the kinematic range the T component remains strongly suppressed compared to the L one. For example, around $q^2 \sim 4 \text{ GeV}^2$, one finds approximately $d\mathcal{B}_L/dq^2 \sim 0.35 \times 10^{-4}$, whereas $d\mathcal{B}_T/dq^2 \sim 0.12 \times 10^{-4}$; however, near the high q^2 or in the last bin, the T contribution becomes slightly dominant, with $d\mathcal{B}_T/dq^2 \sim (0.5-0.6) \times 10^{-5}$ and $d\mathcal{B}_L/dq^2 \sim (0.3-0.4) \times 10^{-5}$. In FIG. 3d, the behavior of the two polarization components differs noticeably. The L contribution exhibits a smooth and relatively large distribution in the range $q^2 \leq 2.4$, whereas the T component stays smaller. Beyond this T become dominant twice as magnitude as L in $q^2 \sim 6-8$ as shown as shown in TABLE III.

- FIG. 3b shows the \mathcal{A}_{FB} for the decay $B^+ \rightarrow D_1\mu\nu$ as a function of q^2 . The L contribution, \mathcal{A}_{FBL} , is positive and sharply enhanced in the very low- q^2 region, reaching about 0.19 near $q^2 \simeq 0$, but then decreases rapidly and remains close to zero over most of the q^2 region. In contrast, the T contribution, \mathcal{A}_{FBT} , is negative throughout the entire q^2 region, decreases to a minimum of about -0.12 around $q^2 \sim 5 \text{ GeV}^2$, and then rises again toward zero near the high q^2 . The unpolarized asymmetry, \mathcal{A}_{FB} , follows the transverse behavior closely, becoming negative after the very low- q^2 region, it crosses zero at approximately $q^2 \sim 0.6 \text{ GeV}^2$, then becomes negative and reaches about -0.10 in the intermediate region before approaching zero near high q^2 region. For FIG. 3e, the behavior follows the same trend as observed in FIG. 3b, but with a comparatively larger magnitude. The distribution reaches its maximum in the bin $q^2 = 3-4 \text{ GeV}^2$, where it lies in the range $(-0.355, -0.368)$. This is roughly an order of magnitude larger than the corresponding values obtained in the negative angle region, which are about $(-0.083, -0.109)$ in the same q^2 bin.
- FIG. 3c and 3f shows the F_L for both angle ranges where the bin-wise values of F_L are listed in the TABLE III show agreement with the plots.

FIG. 4: The polarized and unpolarized branching ratio, lepton forward backward asymmetry, and the longitudinal fraction as a function of q^2 for $B^+ \rightarrow D_1\tau^+\nu$ transition.



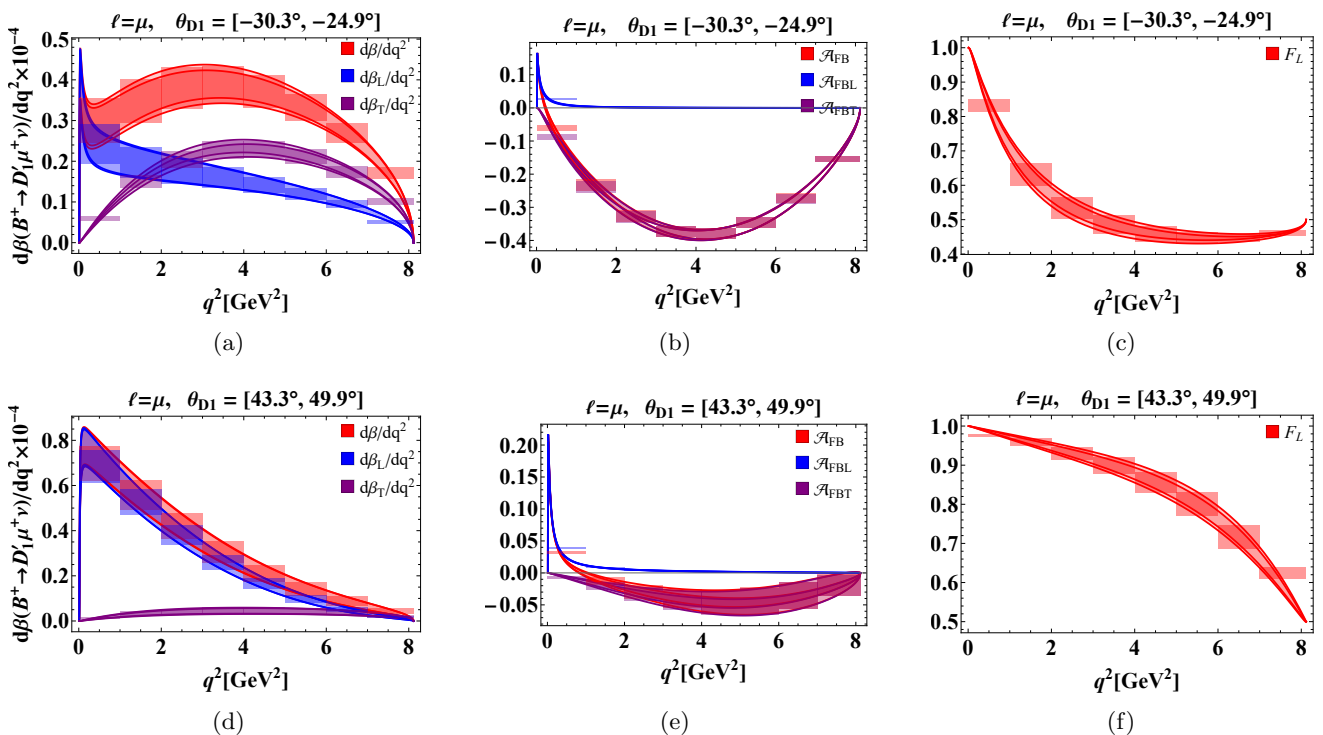
FIGS. 4 displays the q^2 dependence of the different observables for the decay $B^+ \rightarrow D_1\tau^+\nu$, including the branching ratio, the lepton forward-backward asymmetry, and the longitudinal polarization fraction. The results are presented for two representative intervals of the mixing angle: $\theta_{D1} \in [-30.3^\circ, -24.9^\circ]$ (top row) and $\theta_{D1} \in [43.3^\circ, 49.9^\circ]$ (bottom row).

- In FIG. 4a, the differential branching ratio is shown, separating the unpolarized result from the L and T polarization. A clear difference is observed across most of the q^2 region, where the L component provides the leading contribution. In the highest bin, $q^2 \in [7, 8] \text{ GeV}^2$, the T contribution becomes comparable to the T one, with both contributions having similar integrated values in the range $[0.10, 0.13] \times 10^{-5}$. For FIG. 4d, in the positive angle range corresponding to $q^2 \in [7-8] \text{ GeV}^2$, the T contribution becomes larger than the L one, with integrated values $[0.26, 0.29] \times 10^{-5}$ for T and $[0.18, 0.21] \times 10^{-5}$ for L, indicating that the T component dominates near the high q^2 .

- In FIG. 4b, the L and unpolarized components of \mathcal{A}_{FB} remain positive over the entire q^2 region, whereas the T contribution stays negative throughout. The T component is strongly suppressed at low and intermediate q^2 , for example $\mathcal{A}_{\text{FBT}} \simeq -0.01$ around $q^2 \simeq 4 \text{ GeV}^2$, compared with $\mathcal{A}_{\text{FBL}} \simeq 0.16$. However, near the high- q^2 region, its magnitude increases to about 0.05, becoming comparable to the unpolarized contribution as the latter approaches zero. In contrast to FIG. 4b, FIG. 4e shows that the unpolarized \mathcal{A}_{FB} exhibits a zero crossing at approximately $q^2 \simeq 5.3 \text{ GeV}^2$. However, the T contribution remains negative, while the L contribution remains positive throughout the entire q^2 region.
- FIG. 4c and 4f shows the F_L for both angle ranges where the bin-wise values of F_L are listed in the TABLE IV show agreement with the plots.

2. Observable for the decay of $B^+ \rightarrow D_1' \ell^+ \nu_\ell$.

FIG. 5: The polarized and unpolarized branching ratio, lepton forward backward asymmetry, and the longitudinal fraction as a function of q^2 for $B^+ \rightarrow D_1' \mu^+ \nu$ transition.



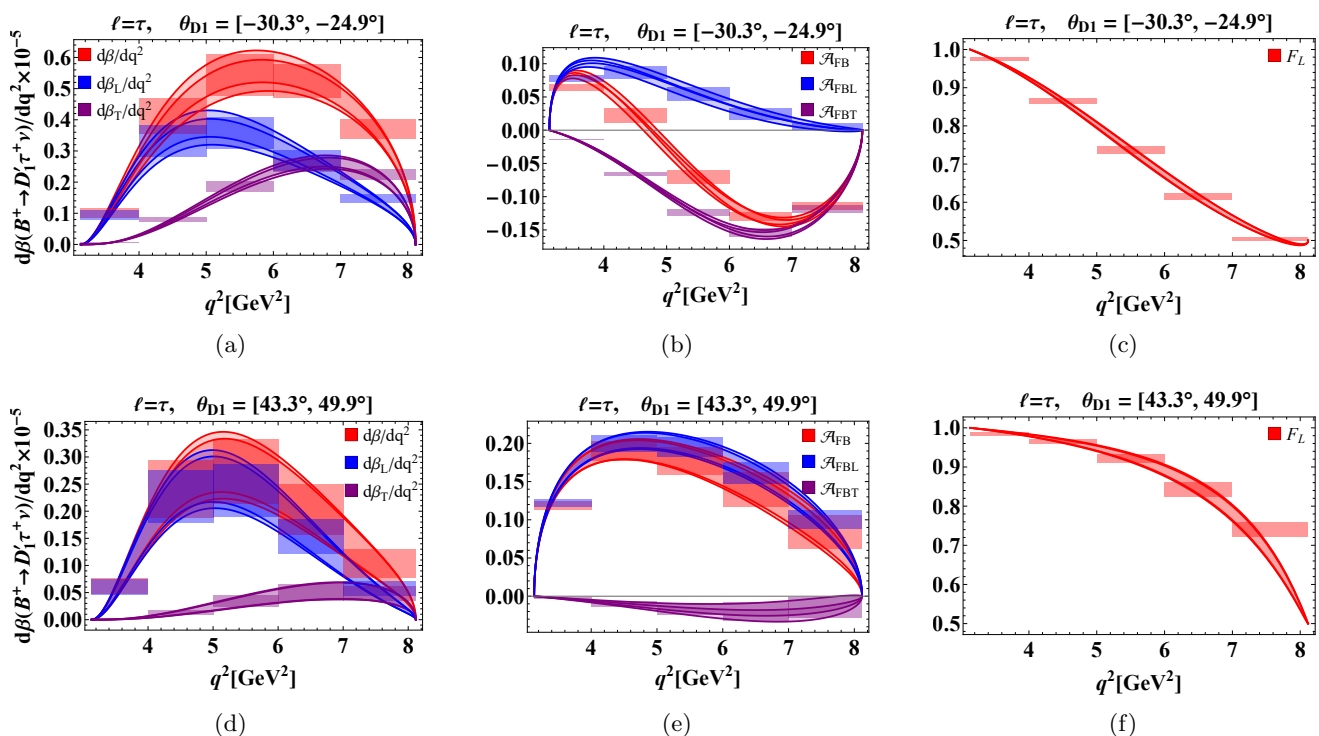
FIGS. 5 depict the q^2 dependence of the different observables for the decay $B^+ \rightarrow D_1' \mu^+ \nu$, including the branching ratio, the \mathcal{A}_{FB} , and the F_L . The results are presented for two representative intervals of the mixing angle: $\theta_{D1} \in [-30.3^\circ, -24.9^\circ]$ (top row) and $\theta_{D1} \in [43.3^\circ, 49.9^\circ]$ (bottom row).

- For FIG. 5a, the L contribution is larger than the T contribution in the low- q^2 region, particularly for $q^2 \lesssim 1.5 \text{ GeV}^2$. However, with increasing q^2 , the T component becomes enhanced and overtakes the L contribution over the intermediate and high- q^2 regions. This indicates a clear change in the polarization hierarchy from L dominance at low q^2 to T dominance at higher q^2 . In contrast, FIG. 5d, shows that the L contribution remains larger than the T contribution over almost the entire q^2 region. The T component is strongly suppressed in this angle range and becomes comparable to the L contribution only near the high q^2 . In the highest integrated bin, $q^2 \in [7, 8] \text{ GeV}^2$, the integrated values are $[0.013, 0.021] \times 10^{-4}$ and $[0.015, 0.027] \times 10^{-4}$ for the L and T

contributions, respectively. Thus, in this endpoint bin, the T contribution becomes comparable to and slightly larger than the L contribution.

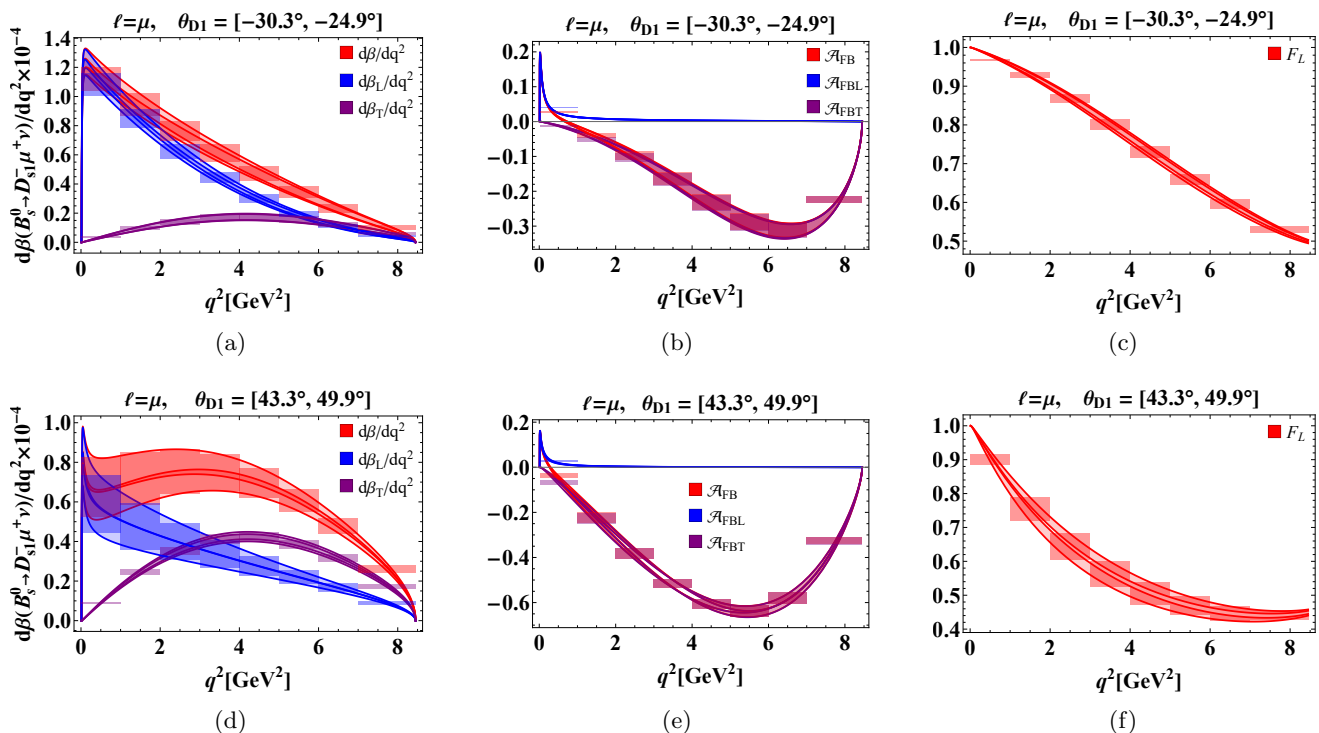
- In FIG. 5b and FIG. 5e, the T component of \mathcal{A}_{FB} dominates over the L contribution throughout the entire q^2 region. In FIG. 5b, the largest magnitude is observed in the range $q^2 \in [4, 5] \text{ GeV}^2$, with values around $[-0.364, -0.395]$, while in FIG. 5e, the maximum occurs near $q^2 \in [5, 6] \text{ GeV}^2$, where \mathcal{A}_{FB} reaches approximately $[-0.024, -0.065]$.
- FIGS. 5c and 5f presents F_L for both angular ranges i.e., $\theta_{D1} \in [-30.3^\circ, -24.9^\circ]$ and $\theta_{D1} \in [43.3^\circ, 49.9^\circ]$. The bin-wise values presented in the TABLE V are consistent with the behavior observed in these plots across the full q^2 region.

FIG. 6: The polarized and unpolarized branching ratio, lepton backward asymmetry, and the longitudinal fraction as a function of q^2 for $B^+ \rightarrow D_1' \tau^+ \nu$ transition.



FIGS. 6 depict the q^2 dependence of the different observables for the decay $B^+ \rightarrow D_1' \tau^+ \nu$, including the branching ratio, the \mathcal{A}_{FB} , and the F_L . The results are presented for two representative intervals of the mixing angle: $\theta_{D1} \in [-30.3^\circ, -24.9^\circ]$ (top row) and $\theta_{D1} \in [43.3^\circ, 49.9^\circ]$ (bottom row).

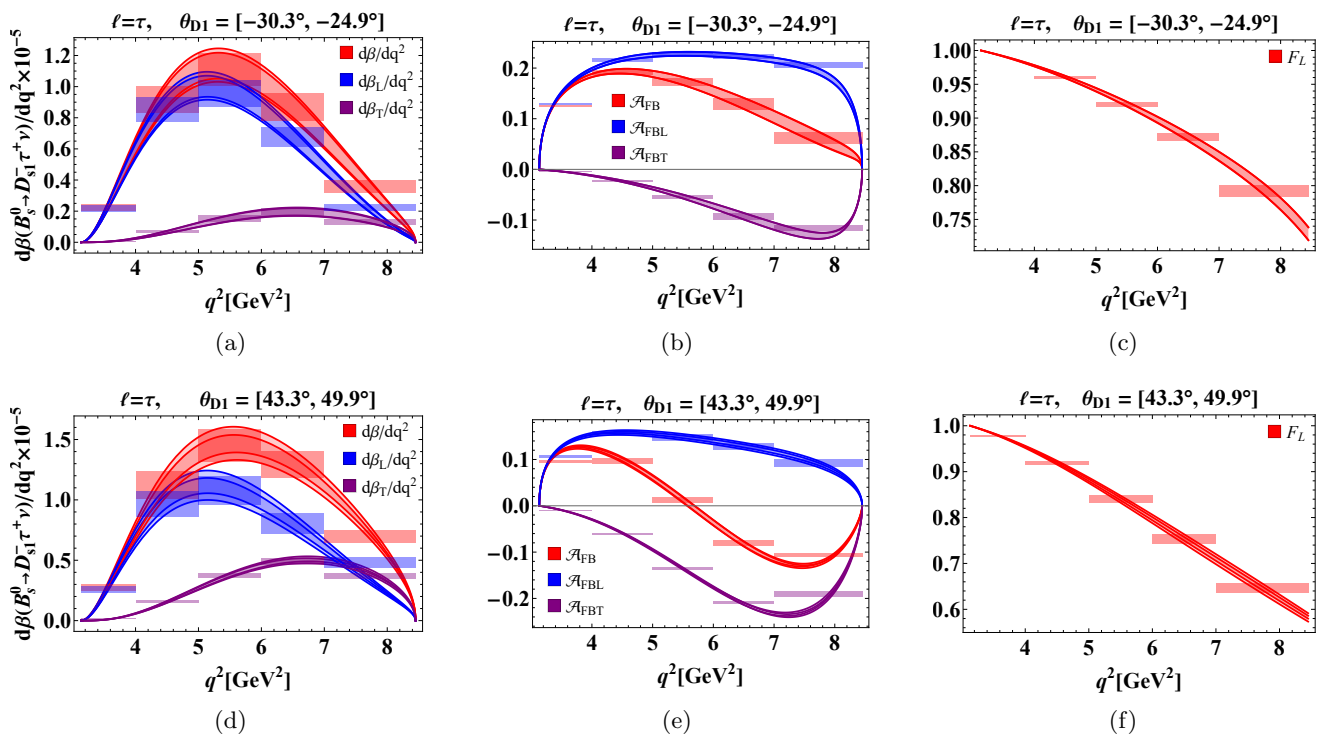
- In FIG. 6a, the L contribution dominates up to approximately $q^2 \simeq 6 \text{ GeV}^2$, beyond which the T component becomes comparable to, and eventually larger than, the L component. The corresponding numerical values in the different q^2 bins are reported in TABLE VI. In contrast, FIG. 6d shows that the L contribution remains the leading polarized component over most of the q^2 region. However, in the highest integrated bin, $q^2 \in [7 - 8] \text{ GeV}^2$, the L and T contributions become comparable, as shown in the plot and listed in TABLE VI.
- The \mathcal{A}_{FB} shows a zero crossing at $q^2 \approx 4.8 \text{ GeV}^2$ as depicted in FIG. 6b. The T component remains small in magnitude and negative throughout the entire q^2 region, indicating a negligible contribution. In contrast, the L contribution is positive and clearly dominant over the full q^2 range.
- FIGS 6c and 6f display F_L for both θ_{D1} ranges, and the bin-wise values presented in the TABLE VI are consistent with the behavior observed in these plots across the full q^2 region.

3. Observable for the decay of $B_s^0 \rightarrow D_{s1}^- \ell^+ \nu_\ell$.FIG. 7: The polarized and unpolarized branching ratio, lepton forward backward asymmetry, and the longitudinal fraction as a function of q^2 for $B^+ \rightarrow D_{s1}^- \mu^+ \nu$ transition.

FIGS. 7 shows the polarized and unpolarized differential branching ratio, \mathcal{A}_{FB} , and the F_L as functions of q^2 for the decay $B^+ \rightarrow D_{s1}^- \mu^+ \nu$. The first row corresponds to the mixing-angle range $\theta_{D1} \in [-30.3^\circ, -24.9^\circ]$, while the second row represents $\theta_{D1} \in [43.3^\circ, 49.9^\circ]$.

- In FIG. 7a, the L component remains larger than the T contribution over most of the q^2 region, particularly in the low and intermediate q^2 regions. However, as q^2 increases, the two polarized contributions become closer in magnitude, especially for $q^2 \gtrsim 6 \text{ GeV}^2$. This behavior is also consistent with the bin-wise numerical values reported in TABLE VII. For FIG. 7d, the polarization pattern is different. The L component dominates only in the low- q^2 region, up to approximately $q^2 \simeq 2.5 \text{ GeV}^2$. Beyond this point, the T contribution becomes larger than the L contribution and remains dominant over the intermediate and high q^2 regions.
- For FIG. 7b, the observable shows a clear dominance of the T contribution over the L one throughout the full kinematic region. The L component remains strongly suppressed and nearly negligible in comparison. Numerically, the bin have higher magnitude fro the T contribution $q^2 = 6-7 \text{ GeV}^2$, reaches values of approximately $(-0.291, -0.333)$, while the L contribution stays much smaller, around $(0.001, 0.002)$. Similarly, FIG. 7e exhibits the same qualitative trend, with the T contribution governing the distribution and the L part remaining suppressed across the entire q^2 region. In the bin $q^2 = 5-6 \text{ GeV}^2$, the T component takes maximum values around $(-0.612, -0.661)$, whereas the L component is significantly smaller, of the order $(\sim 10^{-4})$.
- FIGs 7c and 7f display F_L for both θ_{D1} ranges, and the bin-wise values presented in the TABLE VII are consistent with the behavior observed in these plots across the full q^2 region.

FIG. 8: The polarized and unpolarized branching ratio, lepton forward backward asymmetry, and the longitudinal fraction as a function of q^2 for $B_s^0 \rightarrow D_{s1}^- \tau^+ \nu$ transition.

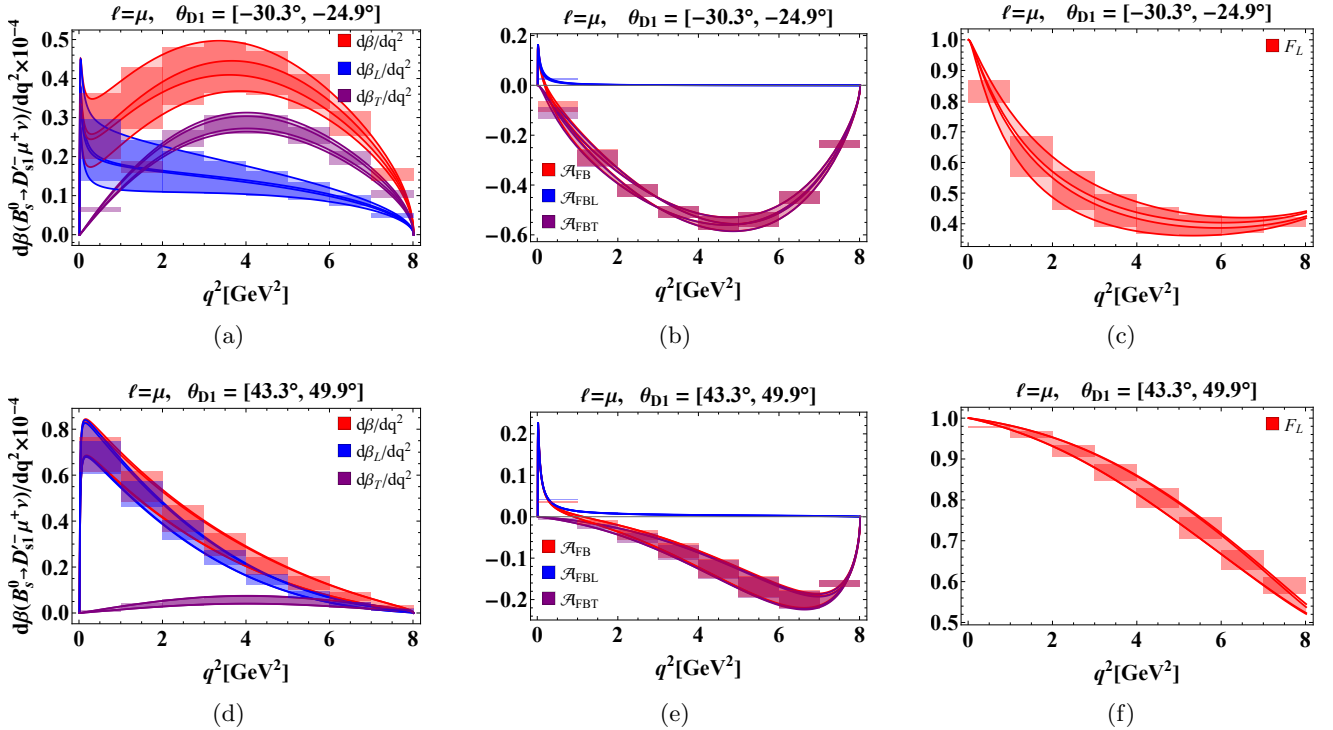


In FIGs. 8, we show the differential branching ratio (polarized and unpolarized), \mathcal{A}_{FB} , and the F_L as functions of q^2 for the process $B^+ \rightarrow D_{s1}^- \tau^+ \nu$. The first (second) row corresponds to $\theta_{D1} \in [-30.3^\circ, -24.9^\circ]$ ($[43.3^\circ, 49.9^\circ]$).

- For FIG. 8a, the L contribution is the dominant polarized component over the whole q^2 region. It rises rapidly from the lower q^2 , reaches its maximum around $q^2 \simeq 5 \text{ GeV}^2$, and then decreases toward the high q^2 . The T contribution is comparatively suppressed throughout the region, although it increases gradually and reaches a small maximum around $q^2 \simeq 6.5 \text{ GeV}^2$. Thus, the L component remains larger than the T component over the full q^2 range. In contrast, FIG. 8d, shows an enhanced transverse contribution compared with the Fig. 8a. The L component still dominates in the low- and intermediate- q^2 regions, but the T component increases significantly with q^2 and becomes comparable to the L component in the high- q^2 region. In particular, near $q^2 \gtrsim 7 \text{ GeV}^2$, the two polarized contributions are close in magnitude, and the T component may slightly exceed the L contribution near the high q^2 . This indicates that the positive mixing angle range leads to a stronger T polarization effect at large q^2 .
- FIG. 8b shows that \mathcal{A}_{FB} follows a behavior similar to that observed in the $B^+ \rightarrow D_1 \tau^+ \nu$ channel in FIG. 4b, with a difference in magnitude. Likewise, FIG. 8e exhibits the same pattern as seen in FIG. 4e, although the numerical values differ. The L and unpolarized components of \mathcal{A}_{FB} remain positive over the entire q^2 range, whereas the T contribution stays negative throughout. In contrast to FIG. 8b, FIG. 8e shows that the unpolarized \mathcal{A}_{FB} exhibits a zero crossing at approximately $q^2 \simeq 5.6 \text{ GeV}^2$. Nevertheless, the T component remains negative, while the L component remains positive across the full q^2 region.
- FIGs 8c and 8f display F_L for both θ_{D1} ranges, and the bin-wise values presented in the TABLE VIII are consistent with the behavior observed in these plots across the full q^2 region.

4. Observable for the decay of $B_s^0 \rightarrow D_{s1}^{-'} \ell^+ \nu_\ell$.

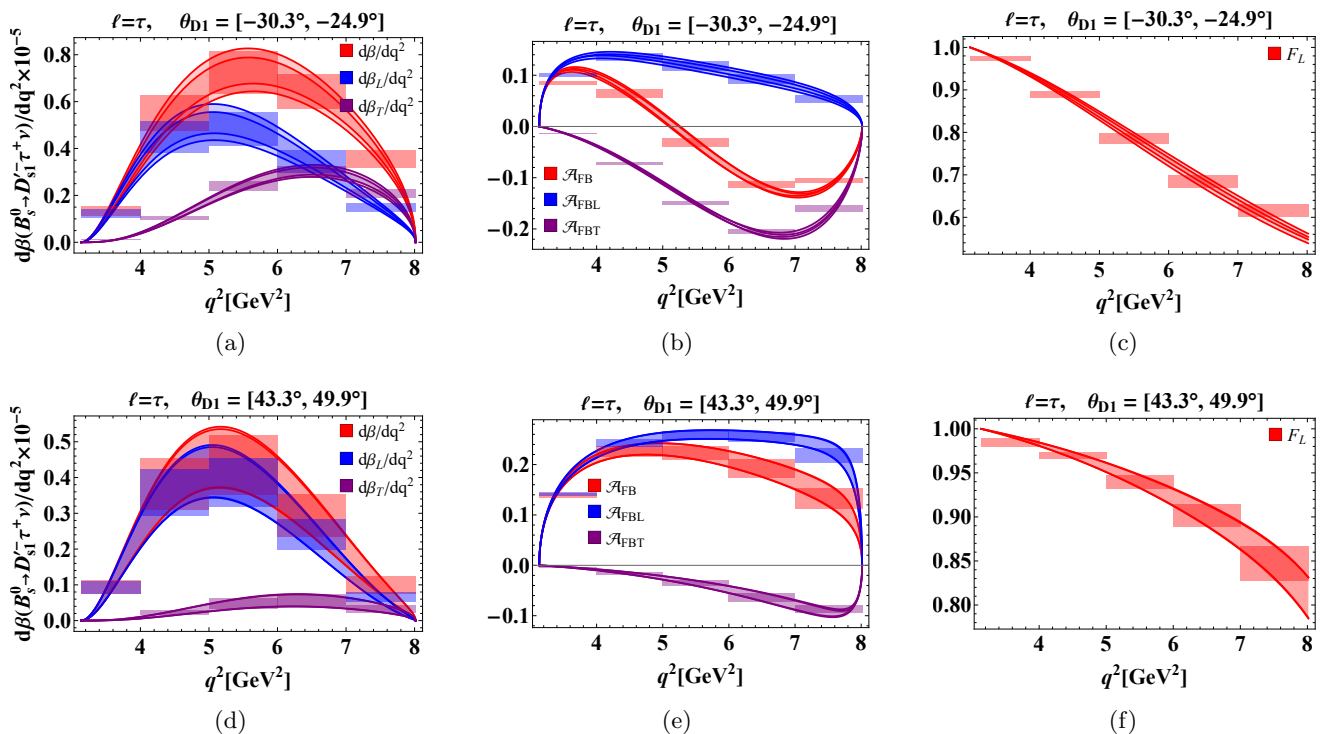
FIG. 9: The polarized and unpolarized branching ratio, lepton forward backward asymmetry, and the longitudinal fraction as a function of q^2 for $B^+ \rightarrow D_{s1}^{\prime} \mu^+ \nu$ transition.



FIGS. 9 illustrates the variation with q^2 of the polarized and unpolarized differential branching ratio, along with the \mathcal{A}_{FB} and the F_L , for the decay $B^+ \rightarrow D_{s1}^{\prime} \mu^+ \nu$. Results are shown for two mixing-angle intervals: $\theta_{D1} \in [-30.3^\circ, -24.9^\circ]$ (top row) and $\theta_{D1} \in [43.3^\circ, 49.9^\circ]$ (bottom row).

- In FIG. 9a, the L contribution dominates in the low- q^2 region, particularly for $q^2 \lesssim 2 \text{ GeV}^2$. As q^2 increases, the T component grows and becomes dominant in the intermediate and high- q^2 regions, indicating a transition from L to T dominance. In contrast, FIG. 9d shows that the L contribution remains dominant over most of the q^2 range, with the T component significantly suppressed and becoming comparable only near the high- q^2 bin. In the highest bin, $q^2 \in [6 - 8] \text{ GeV}^2$, the integrated values are $[0.013, 0.060] \times 10^{-4}$ and $[0.015, 0.027] \times 10^{-4}$ for the L and T contributions, respectively, indicating that the T contribution slightly exceeds the L one in this region.
- In FIG. 9b and FIG. 9e, corresponding to the \mathcal{A}_{FB} the T component dominates over the L contribution across the entire q^2 region. In FIG. 9b, the largest magnitude occurs in the range $q^2 \in [4 - 5] \text{ GeV}^2$, with values around $[-0.52, -0.57]$, while in FIG. 9e, the maximum is observed near $q^2 \in [6 - 7] \text{ GeV}^2$, where \mathcal{A}_{FB} reaches approximately $[-0.17, -0.22]$.
- The longitudinal polarization fraction F_L , presented in FIGS. 9c and 9f, follows a behavior that is consistent with the bin-integrated results given in TABLE IX for both θ_{D1} ranges across the full q^2 range.

FIG. 10: The polarized and unpolarized branching ratio, lepton forward backward asymmetry, and the longitudinal fraction as a function of q^2 for $B^+ \rightarrow D'_{s1} \tau^+ \nu$ transition.

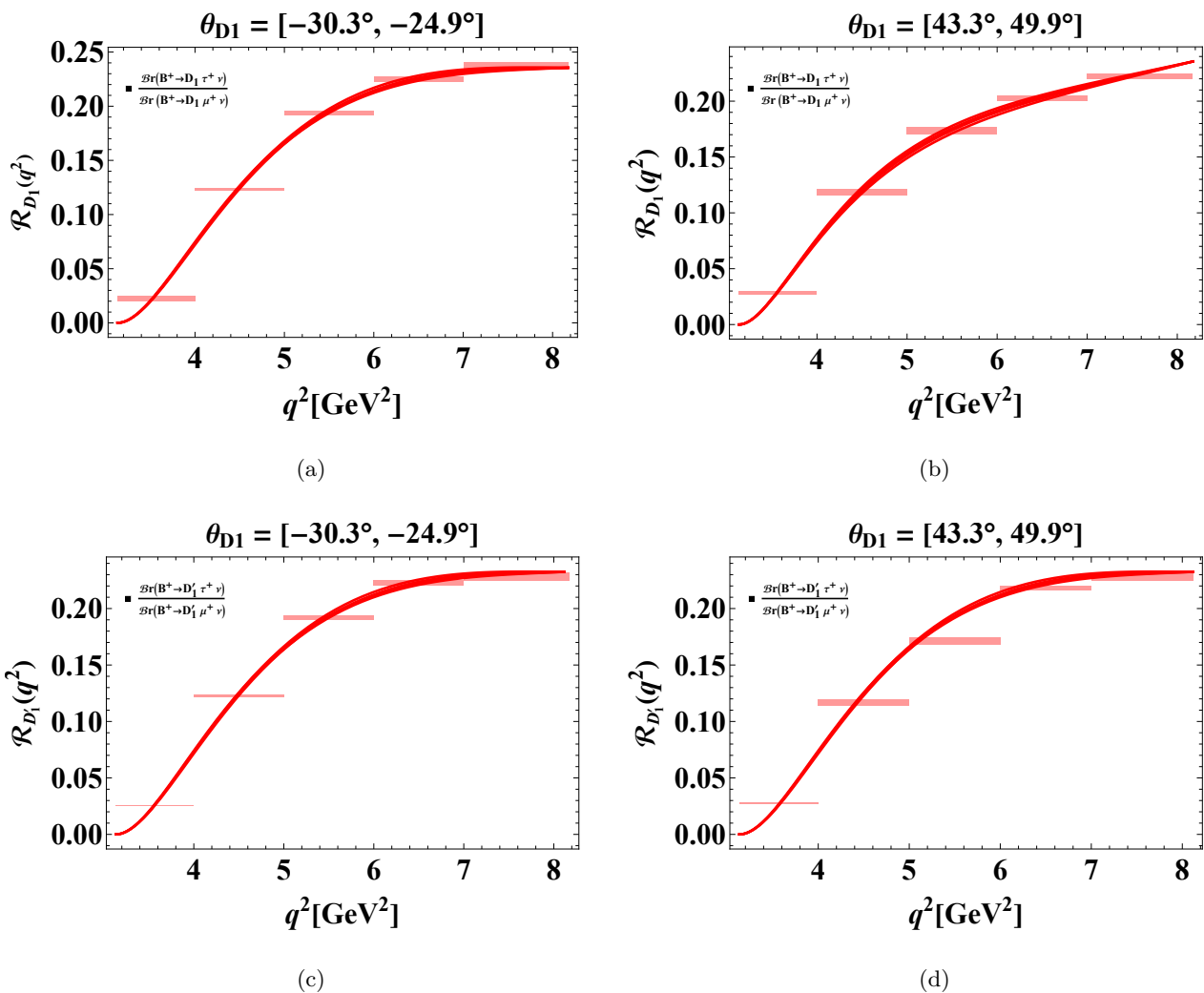


The q^2 distributions of the polarized and unpolarized differential branching ratio, \mathcal{A}_{FB} and the F_L for $B^+ \rightarrow D'_{s1} \tau^+ \nu$ are displayed in FIGs. 10. The results are presented for two mixing-angle regions: $\theta_{D1} \in [-30.3^\circ, -24.9^\circ]$ (upper row) and $\theta_{D1} \in [43.3^\circ, 49.9^\circ]$ (lower row).

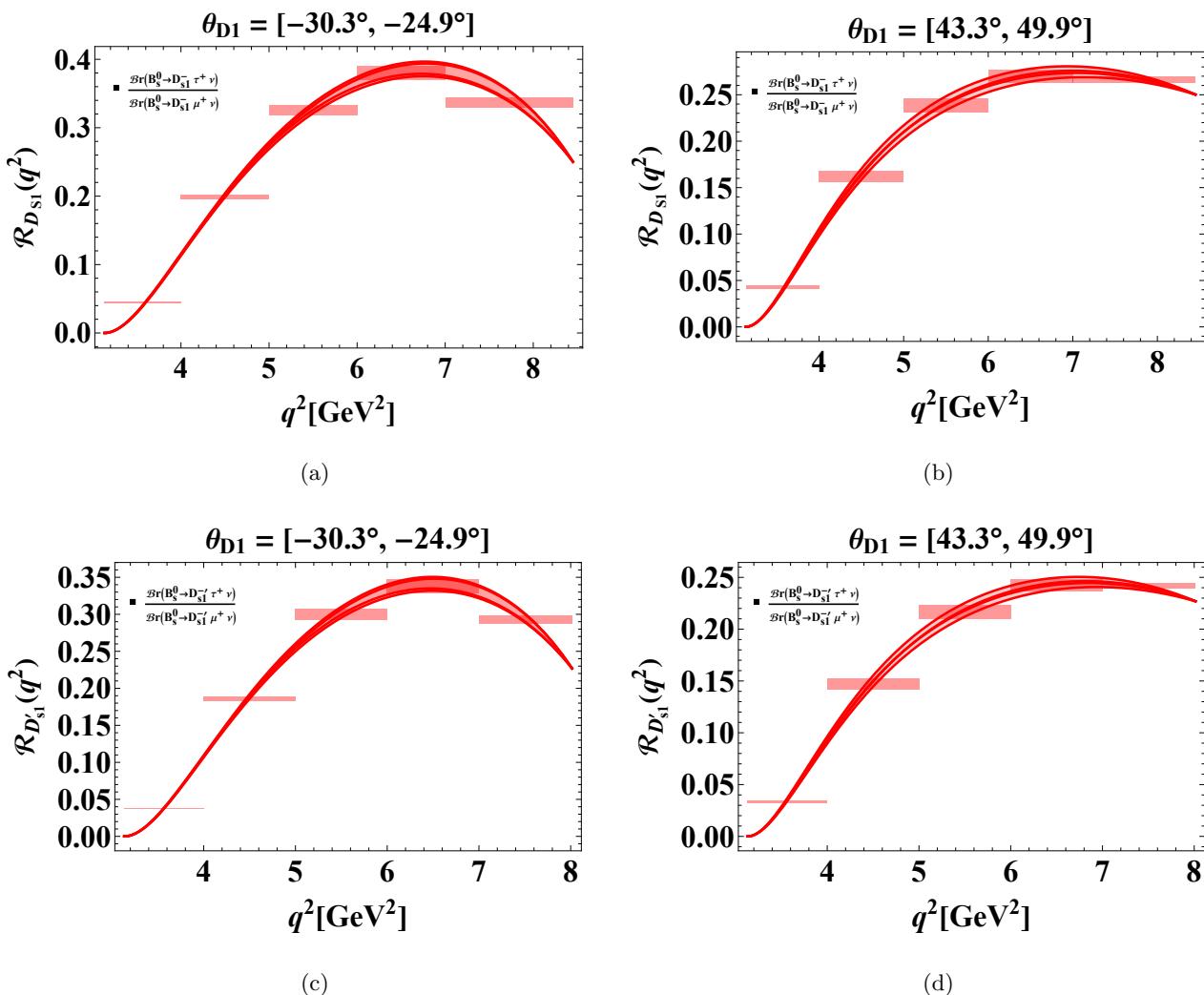
- In FIG. 10a, corresponding to the branching ratio the L contribution dominates up to approximately $q^2 \leq 6.5 \text{ GeV}^2$. Beyond this region, the T component increases and becomes comparable to, and eventually slightly larger than, the L contribution at higher q^2 . This behavior closely follows that observed in the D'_1 channel, with only differences in the numerical values. The corresponding bin-wise values are listed in TABLE X. In contrast, FIG. 10d show the L contribution remains dominant over most of the q^2 region. However, in the slight highest bin, $q^2 \geq 7.5 \text{ GeV}^2$, the L and T contributions become comparable, as also reflected in TABLE X. This trend is again consistent with the behavior seen in the D'_1 case.
- The \mathcal{A}_{FB} , shown in FIG. 10b, unpolarized exhibits a zero crossing at around $q^2 \approx 5.1 \text{ GeV}^2$. The transverse component remains positive and T remain negative over the entire q^2 region. A similar pattern is observed in FIG. 6e, where the qualitative features remain unchanged compared to the D'_1 channel, with only numerical differences.
- FIGs. 10c and 10f show the variation of F_L for both θ_{D1} ranges. The bin-wise values listed in TABLE X are in good agreement with the trends observed in the plots over the entire q^2 region.

5. The Ratio of Branching Fraction

Ratios of branching fractions such as $\mathcal{R}_{(D)}$ [79–81] and $\mathcal{R}_{(D^*)}$ [80, 82, 83] have been studied in both experimental and theoretical literature as sensitive probes of LFU [84–87]. Therefore, in this work, we extend the study of $\mathcal{R}_{D_1^{(\prime)}}$ and $\mathcal{R}_{D_{s1}^{(\prime)}}$ observables define in Eq. (12) as a complementary check on LFU.

FIG. 11: The ratio of the branching fraction \mathcal{R}_{D_1} and $\mathcal{R}_{D'_1}$ as a function of q^2 .

FIGs. 11a and 11b show the q^2 dependence of the ratio $\mathcal{R}(q^2)$ for the $B^+ \rightarrow D_1$ channel, while FIGs 11c and 11d correspond to the $B^+ \rightarrow D'_1$ channel. The results are presented for both negative $\theta_{D1} \in [-30.3^\circ, -24.9^\circ]$ and positive $\theta_{D1} \in [43.3^\circ, 49.9^\circ]$ mixing angle ranges. The bin-wise values of the ratio are listed in TABLE XI.

FIG. 12: The ratio of the branching fraction $\mathcal{R}_{D_{s1}}$ and $\mathcal{R}_{D'_{s1}}$ as a function of q^2 .

FIGs. 12a and 12b show the q^2 dependence of the ratio $\mathcal{R}(q^2)$ for the $B_s^0 \rightarrow D_{s1}$ channel, while FIGs 12c and 12d correspond to the $B_s^0 \rightarrow D'_{s1}$ channel. The results are presented for both negative $\theta_{D1} \in [-30.3^\circ, -24.9^\circ]$ and positive $\theta_{D1} \in [43.3^\circ, 49.9^\circ]$ mixing angle ranges. The bin-wise values of the ratio are listed in TABLE XI.

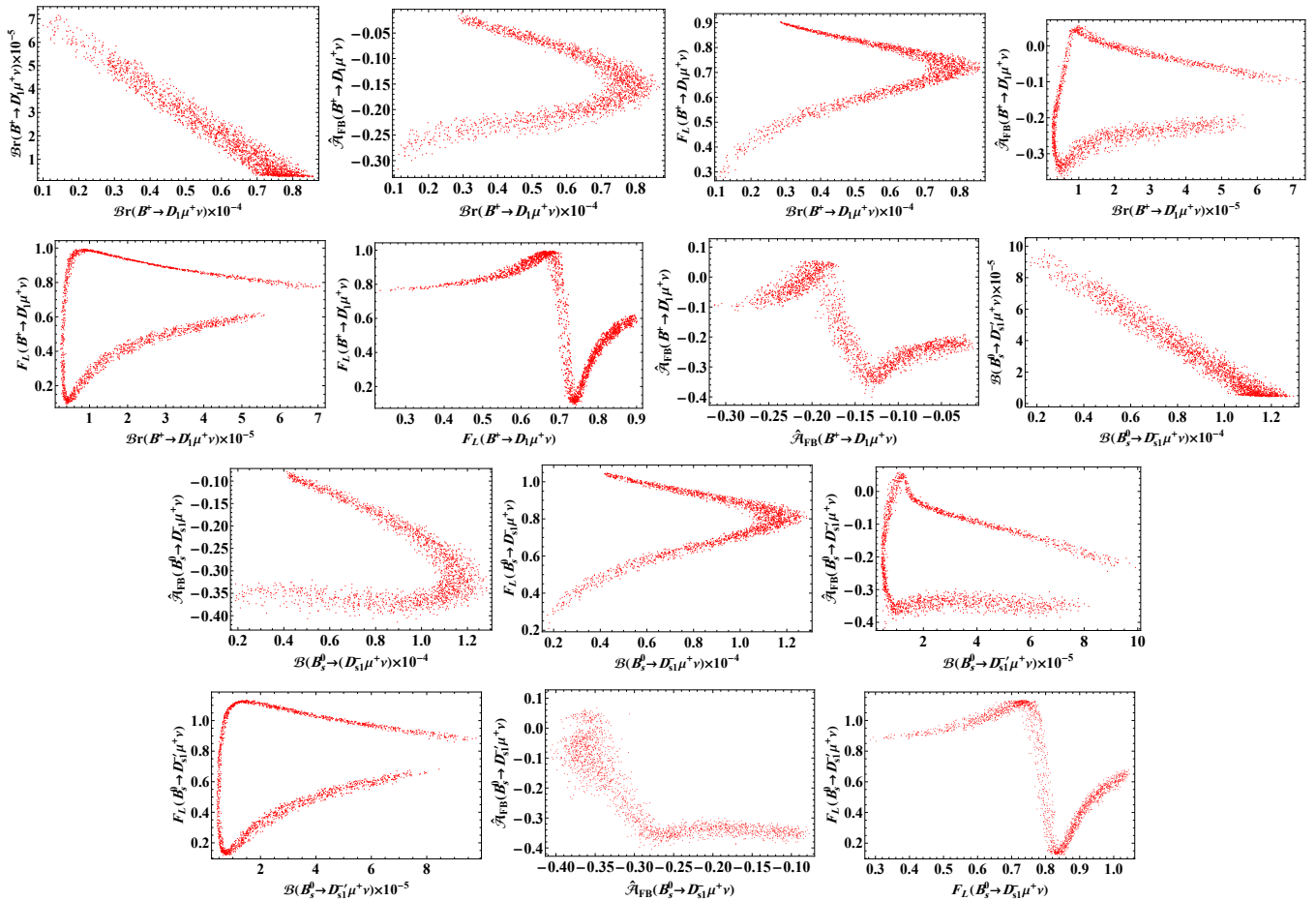
In Figs. 11 and 12, for both cases, the ratios are suppressed in the low- q^2 region because of the reduced phase space available for the τ mode, and then increase toward higher q^2 . The bin-averaged points, together with their uncertainties, follow the same overall behavior as the continuous curves, showing that the overall trend is stable within the theoretical uncertainties. Since these ratios are constructed from the same hadronic transition in the τ and μ modes, part of the hadronic form-factor uncertainties cancels between numerator and denominator, making \mathcal{R}_{D_1} and $\mathcal{R}_{D_{s1}}$ theoretically cleaner than the individual branching ratios.

C. Correlation Analysis for $B^+ \rightarrow D_1^{(\prime)} \ell^+ \nu_\ell$ and $B_s^0 \rightarrow D_{s1}^{(\prime)} \ell^+ \nu_\ell$ Decays

In this section, we analyze the correlations among the key observables, namely the branching ratio $d\mathcal{B}/dq^2$, the lepton forward-backward asymmetry \mathcal{A}_{FB} , and the longitudinal polarization fraction F_L , for the decay channels $B^+ \rightarrow D_1 \mu^+ \nu_\mu$ and $B^+ \rightarrow D'_1 \mu^+ \nu_\mu$. These correlations are obtained by scanning over the full allowed range of the mixing angle $\theta_{D1} \sim [-45.0^\circ, 80.0^\circ]$ are shown in FIG. 13. The branching ratios of the two mixed axial vector states show an anti-correlated behavior, reflecting the complementary contributions of the $j_\ell = 1/2$ and $j_\ell = 3/2$

components. The correlations involving \mathcal{A}_{FB} and F_L show a curved structures rather than simple linear trends, indicating that these observables are strongly affected by the variation of the mixing angle. Overall, the correlation patterns show that the branching ratios, forward backward asymmetries, and longitudinal polarization fractions provide complementary sensitivity to the axial vector mixing structure.

FIG. 13: Correlations between observables for the decay channels $B^+ \rightarrow D_1\mu^+\nu$, $B^+ \rightarrow D_1'\mu^+\nu$, $B_s^0 \rightarrow D_{s1}^-\mu^+\nu$ and $B_s^0 \rightarrow D_{s1}'^-\mu^+\nu$.



IV. CONCLUSION

In this work, we have investigated the $b \rightarrow c\ell\nu$ mediated B decays $B^+ \rightarrow D_1^{(\prime)}\ell^+\nu_\ell$ and $B_s^0 \rightarrow D_{s1}^{-(\prime)}\ell^+\nu_\ell$, where $\ell = \mu$ and τ within the SM framework, using the effective weak Hamiltonian. The physical axial vector states $D_1^{(\prime)}$ and $D_{s1}^{(\prime)}$ are treated as mixtures of the $D_1^{3/2}$ and $D_1^{1/2}$ states, respectively, and the dependence on the mixing angle θ_{D1} is explicitly taken into account. The elements of the hadronic matrix associated with the $B^+ \rightarrow D_1^{(\prime)}\ell^+\nu_\ell$ and $B_s^0 \rightarrow D_{s1}^{-(\prime)}\ell^+\nu_\ell$ transition are parametrized in terms of the helicity form factors that are dependent on q^2 . By using CLFQM form factors we have numerically calculated the differential branching ratio $d\mathcal{B}/dq^2$, the longitudinal polarization fraction F_L , the lepton forward-backward asymmetry \mathcal{A}_{FB} , and the lepton flavor universality ratios $R_{D_1^{(\prime)}}$ and $R_{D_{s1}^{(\prime)}}$. We have also presented the polarized branching ratios and forward backward asymmetries corresponding to longitudinal and transverse final state mesons. The numerical analysis is carried out by considering the mixing angle in two regions, $\theta_{D1} \in [-30.3^\circ, -24.9^\circ]$ and $\theta_{D1} \in [43.3^\circ, 49.9^\circ]$. We sequentially discuss the implications of the $d\mathcal{B}/dq^2$ (polarized and unpolarized), \mathcal{A}_{FB} (polarized and unpolarized) and F_L over entire wide range of angles. At present, experimental data are available only for the branching ratios of the $B^+ \rightarrow D_1^{(\prime)}\ell^+\nu_\ell$ channels. In addition to these, we provide detailed predictions for the corresponding observables in the $B_s^0 \rightarrow D_{s1}^{-(\prime)}\ell^+\nu_\ell$ channels, for which no experimental measurements are currently available. These results offer a consistent SM baseline and can serve as important inputs for future experimental studies, helping to test the sensitivity of different observables to the mixing angle and to further clarify the existing tension between theoretical predictions and experimental observations. Furthermore, we have presented bin averaged predictions of the observables using a bin width of $\Delta q^2 = 1 \text{ GeV}^2$, which are particularly useful for future experimental analyses. Finally, our study extends the analysis to the $R_{D_1^{(\prime)}}$ and $R_{D_{s1}^{(\prime)}}$ observables as complementary probes of LFU, and also discusses the correlations among different observables. Precise measurements of these observables, together with polarization-dependent quantities, will not only help constrain the mixing angle but also provide deeper insight into the existing tensions between theoretical predictions and experimental observations, thereby offering an important avenue for testing the SM in semileptonic $b \rightarrow c\ell\nu$ transitions.

APPENDIX

TABLE III: Predictions of binned observables for the decay channel $B^+ \rightarrow D_1 \mu^+ \nu$, including unpolarized differential branching ratio $\langle d\mathcal{B}/dq^2 \rangle$, the lepton forward-backward asymmetry $\langle \mathcal{A}_{\text{FB}} \rangle$ and longitudinal polarization fraction (F_L) is given within the SM framework in $\Delta q^2 \sim 1$ bins. The differential branching ratio and the lepton forward backward asymmetry are also given with the final state meson is longitudinal and transverse polarized. The upper value in the table correspond to the negative angle range $[-30.3^\circ, -24.9^\circ]$, while the second value corresponds to positive angle range $\theta_{D1} \in [43.3^\circ, 49.9^\circ]$. The differential branching ratios are given in order of 10^{-4} GeV^{-2} .

[$-30.3^\circ, -24.9^\circ$]							
$q^2 = \text{GeV}^2$	$\langle d\mathcal{B}/dq^2 \rangle$	$\langle d\mathcal{B}_L/dq^2 \rangle$	$\langle d\mathcal{B}_T/dq^2 \rangle$	$\langle \hat{\mathcal{A}}_{\text{FB}} \rangle$	$\langle \hat{\mathcal{A}}_{\text{FBL}} \rangle$	$\langle \hat{\mathcal{A}}_{\text{FBT}} \rangle$	$\langle \hat{F}_L \rangle$
[0.01 – 1]	(0.993, 1.096)	(0.963, 1.057)	(0.029, 0.039)	(0.021, 0.025)	(0.036, 0.037)	(-0.012, -0.015)	(0.961, 0.966)
[1 – 2]	(0.824, 0.922)	(0.750, 0.825)	(0.073, 0.097)	(-0.031, -0.043)	(0.007, 0.008)	(-0.039, -0.050)	(0.918, 0.0931)
[2 – 3]	(0.652, 0.744)	(0.555, 0.616)	(0.096, 0.128)	(-0.060, -0.080)	(0.003, 0.004)	(-0.064, -0.083)	(0.866, 0.887)
[3 – 4]	(0.503, 0.585)	(0.396, 0.445)	(0.106, 0.140)	(-0.080, -0.107)	(0.001, 0.002)	(-0.083, -0.109)	(0.815, 0.840)
[4 – 5]	(0.376, 0.448)	(0.269, 0.307)	(0.107, 0.140)	(-0.091, -0.122)	(0.001, 0.0012)	(-0.092, -0.123)	(0.760, 0.788)
[5 – 6]	(0.272, 0.330)	(0.117, 0.199)	(0.100, 0.131)	(-0.091, -0.122)	($\sim 10^{-4}$)	(-0.093, -0.123)	(0.698, 0.726)
[6 – 7]	(0.183, 0.228)	(0.097, 0.116)	(0.086, 0.111)	(-0.078, -0.104)	($\sim 10^{-4}$)	(-0.078, -0.105)	(0.626, 0.651)
[7 – 8.17]	(0.105, 0.133)	(0.043, 0.054)	(0.061, 0.078)	(-0.051, -0.069)	($\sim 10^{-4}$)	(-0.052, -0.069)	(0.530, 0.540)
[$43.3^\circ, 49.9^\circ$]							
[0.01 – 1]	(0.563, 0.727)	(0.489, 0.641)	(0.074, 0.085)	(-0.025, -0.034)	(-0.031, 0.028)	(-0.055, -0.065)	(0.881, 0.899)
[1 – 2]	(0.586, 0.730)	(0.394, 0.511)	(0.191, 0.219)	(-0.173, -0.197)	(0.004, 0.004)	(-0.178, -0.202)	(0.725, 0.763)
[2 – 3]	(0.595, 0.721)	(0.336, 0.426)	(0.259, 0.294)	(-0.274, -0.304)	(0.001, 0.002)	(-0.276, -0.306)	(0.626, 0.667)
[3 – 4]	(0.575, 0.681)	(0.284, 0.353)	(0.290, 0.327)	(-0.335, -0.367)	($\sim 10^{-4}$)	(-0.355, -0.368)	(0.563, 0.602)
[4 – 5]	(0.529, 0.615)	(0.236, 0.286)	(0.293, 0.328)	(-0.354, -0.386)	($\sim 10^{-4}$)	(-0.330, -0.386)	(0.522, 0.556)
[5 – 6]	(0.461, 0.527)	(0.189, 0.223)	(0.272, 0.303)	(-0.330, -0.360)	($\sim 10^{-4}$)	(-0.264, -0.360)	(0.494, 0.521)
[6 – 7]	(0.368, 0.414)	(0.139, 0.160)	(0.228, 0.253)	(-0.263, -0.288)	($\sim 10^{-4}$)	(-0.155, -0.289)	(0.477, 0.496)
[7 – 8.17]	(0.243, 0.269)	(0.085, 0.095)	(0.157, 0.173)	(-0.155, -0.171)	($\sim 10^{-4}$)	(-0.155, -0.171)	(0.480, 0.490)

TABLE IV: Same as in Table III but for $B^+ \rightarrow D_1 \tau^+ \nu$. The differential branching ratios are given in order of 10^{-5} GeV^{-2} .

[$-30.3^\circ, -24.9^\circ$]							
$q^2 = \text{GeV}^2$	$\langle d\mathcal{B}/dq^2 \rangle$	$\langle d\mathcal{B}_L/dq^2 \rangle$	$\langle d\mathcal{B}_T/dq^2 \rangle$	$\langle \hat{\mathcal{A}}_{\text{FB}} \rangle$	$\langle \hat{\mathcal{A}}_{\text{FBL}} \rangle$	$\langle \hat{\mathcal{A}}_{\text{FBT}} \rangle$	$\langle \hat{F}_L \rangle$
[3.13 – 4]	(0.011, 0.014)	(0.011, 0.013)	($\sim 10^{-4}$)	(0.101, 0.105)	(0.105, 0.109)	(-0.004, -0.005)	(0.970, 0.980)
[4 – 5]	(0.045, 0.054)	(0.041, 0.051)	(0.003, 0.004)	(0.142, 0.152)	(0.163, 0.171)	(-0.018, -0.022)	(0.945, 0.951)
[5 – 6]	(0.052, 0.063)	(0.043, 0.052)	(0.008, 0.011)	(0.108, 0.126)	(0.150, 0.160)	(-0.033, -0.042)	(0.880, 0.892)
[6 – 7]	(0.041, 0.050)	(0.029, 0.035)	(0.012, 0.015)	(0.058, 0.080)	(0.115, 0.126)	(-0.441, -0.057)	(0.780, 0.797)
[7 – 8.17]	(0.020, 0.026)	(0.10, 0.013)	(0.010, 0.013)	(0.013, 0.032)	(0.067, 0.075)	(-0.041, -0.054)	(0.680, 0.700)
[$43.3^\circ, 49.9^\circ$]							
[3.13 – 4]	(0.015, 0.018)	(0.014, 0.017)	(0.001, 0.002)	(0.069, 0.076)	(0.081, 0.008)	(-0.010, -0.011)	(0.930, 0.940)
[4 – 5]	(0.060, 0.073)	(0.050, 0.062)	(0.009, 0.011)	(0.043, 0.057)	(0.099, 0.112)	(0.053, -0.057)	(0.887, 0.895)
[5 – 6]	(0.078, 0.092)	(0.054, 0.066)	(0.023, 0.026)	(-0.027, -0.041)	(0.069, 0.084)	(-0.107, -0.115)	(0.772, 0.786)
[6 – 7]	(0.073, 0.084)	(0.040, 0.047)	(0.033, 0.036)	(-0.093, -0.106)	(0.037, 0.050)	(-0.038, -0.050)	(0.650, 0.664)
[7 – 8.17]	(0.045, 0.051)	(0.018, 0.021)	(0.026, 0.029)	(-0.096, -0.108)	(0.013, 0.021)	(-0.114, -0.125)	(0.501, 0.511)

TABLE V: Same as in Table III but for $B^+ \rightarrow D'_1 \mu^+ \nu$. The differential branching ratios are given in order of 10^{-4} GeV^{-2} .

[$-30.3^\circ, -24.9^\circ$]							
$q^2 = \text{GeV}$	$\langle d\mathcal{B}/dq^2 \rangle$	$\langle d\mathcal{B}_L/dq^2 \rangle$	$\langle d\mathcal{B}_T/dq^2 \rangle$	$\langle \hat{\mathcal{A}}_{\text{FB}} \rangle$	$\langle \hat{\mathcal{A}}_{\text{FBL}} \rangle$	$\langle \hat{\mathcal{A}}_{\text{FBT}} \rangle$	$\langle \hat{F}_L \rangle$
[0.01 – 1]	(0.245, 0.355)	(0.193, 0.290)	(0.052, 0.064)	(-0.052, -0.069)	(0.025, 0.029)	(-0.079, -0.097)	(0.813, 0.850)
[1 – 2]	(0.293, 0.399)	(0.158, 0.233)	(0.135, 0.165)	(-0.217, -0.250)	(0.002, 0.003)	(-0.220, -0.254)	(0.599, 0.665)
[2 – 3]	(0.330, 0.431)	(0.146, 0.207)	(0.184, 0.224)	(-0.309, -0.344)	(0.001, 0.002)	(-0.311, -0.345)	(0.503, 0.566)
[3 – 4]	(0.341, 0.433)	(0.134, 0.184)	(0.206, 0.249)	(-0.357, -0.389)	($\sim 10^{-4}$)	(-0.357, -0.390)	(0.457, 0.511)
[4 – 5]	(0.330, 0.409)	(0.122, 0.160)	(0.208, 0.249)	(-0.363, 0.395)	($\sim 10^{-4}$)	(-0.330, -0.395)	(0.437, 0.481)
[5 – 6]	(0.299, 0.363)	(0.105, 0.134)	(0.193, 0.228)	(-0.330, -0.361)	($\sim 10^{-4}$)	(-0.330, -0.361)	(0.430, 0.464)
[6 – 7]	(0.244, 0.291)	(0.084, 0.103)	(0.160, 0.188)	(-0.147, -0.163)	($\sim 10^{-4}$)	(-0.259, -0.287)	(0.435, 0.458)
[7 – 8.11]	(0.156, 0.183)	(0.047, 0.056)	(0.092, 0.108)	(-0.147, -0.163)	($\sim 10^{-5}$)	(-0.147, -0.163)	(0.450, 0.470)
[$43.3^\circ, 49.9^\circ$]							
[0.01 – 1]	(0.619, 0.772)	(0.755, 0.610)	(0.008, 0.016)	(0.030, 0.034)	(0.038, 0.040)	(-0.005, -0.008)	(0.972, 0.978)
[1 – 2]	(0.493, 0.625)	(0.472, 0.583)	(0.020, 0.041)	(-0.007, -0.019)	(0.007, 0.008)	(-0.015, -0.027)	(0.949, 0.968)
[2 – 3]	(0.362, 0.476)	(0.335, 0.422)	(0.027, 0.053)	(-0.018, -0.039)	(0.003, 0.004)	(-0.023, -0.044)	(0.914, 0.946)
[3 – 4]	(0.256, 0.350)	(0.226, 0.292)	(0.030, 0.058)	(-0.025, -0.054)	(0.001, 0.002)	(-0.028, -0.057)	(0.876, 0.919)
[4 – 5]	(0.174, 0.249)	(0.143, 0.190)	(0.030, 0.058)	(-0.026, -0.063)	(0.001, 0.002)	(-0.028, -0.065)	(0.830, 0.883)
[5 – 6]	(0.112, 0.169)	(0.082, 0.115)	(0.029, 0.054)	(-0.023, -0.064)	(0.001, 0.002)	(-0.024, -0.065)	(0.796, 0.830)
[6 – 7]	(0.066, 0.107)	(0.040, 0.060)	(0.025, 0.046)	(-0.014, -0.055)	($\sim 10^{-4}$)	(-0.015, -0.056)	(0.687, 0.747)
[7 – 8.11]	(0.031, 0.055)	(0.013, 0.021)	(0.015, 0.027)	(-0.002, -0.035)	($\sim 10^{-4}$)	(-0.002, -0.035)	(0.610, 0.640)

TABLE VI: Same as in Table IV but for $B^+ \rightarrow D'_1 \tau^+ \nu$. The differential branching ratios are given in order of 10^{-5} GeV^{-2} .

[$-30.3^\circ, -24.9^\circ$]							
$q^2 = \text{GeV}$	$\langle d\mathcal{B}/dq^2 \rangle$	$\langle d\mathcal{B}_L/dq^2 \rangle$	$\langle d\mathcal{B}_T/dq^2 \rangle$	$\langle \hat{\mathcal{A}}_{\text{FB}} \rangle$	$\langle \hat{\mathcal{A}}_{\text{FBL}} \rangle$	$\langle \hat{\mathcal{A}}_{\text{FBT}} \rangle$	$\langle \hat{F}_L \rangle$
[3.13 – 4]	(0.086, 0.117)	(0.079, 0.109)	(0.006, 0.008)	(0.058, 0.068)	(0.072, 0.082)	(-0.013, -0.014)	(0.970, 0.980)
[4 – 5]	(0.352, 0.478)	(0.281, 0.382)	(0.071, 0.085)	(0.011, 0.032)	(0.078, 0.096)	(-0.062, -0.067)	(0.857, 0.871)
[5 – 6]	(0.477, 0.610)	(0.306, 0.407)	(0.170, 0.203)	(-0.060, -0.080)	(0.043, 0.063)	(-0.119, -0.128)	(0.727, 0.746)
[6 – 7]	(0.469, 0.578)	(0.235, 0.302)	(0.234, 0.276)	(-0.123, -0.135)	(0.015, 0.032)	(-0.147, -0.160)	(0.605, 0.622)
[7 – 8.11]	(0.339, 0.402)	(0.132, 0.161)	(0.206, 0.241)	(-0.107, -0.119)	(0.001, 0.009)	(-0.113, -0.125)	(0.501, 0.511)
[$43.3^\circ, 49.9^\circ$]							
[3.13 – 4]	(0.047, 0.076)	(0.074, 0.046)	(0.001, 0.002)	(0.113, 0.124)	(0.116, 0.126)	(-0.002, -0.003)	(0.981, 0.990)
[4 – 5]	(0.188, 0.294)	(0.179, 0.276)	(0.009, 0.018)	(0.176, 0.202)	(0.189, 0.210)	(-0.006, -0.013)	(0.960, 0.971)
[5 – 6]	(0.213, 0.332)	(0.190, 0.287)	(0.023, 0.045)	(0.159, 0.195)	(0.181, 0.207)	(-0.009, -0.024)	(0.911, 0.933)
[6 – 7]	(0.156, 0.249)	(0.121, 0.184)	(0.035, 0.065)	(0.117, 0.162)	(0.146, 0.175)	(-0.008, -0.032)	(0.824, 0.861)
[7 – 8.11]	(0.077, 0.131)	(0.043, 0.070)	(0.033, 0.061)	(0.061, 0.105)	(0.087, 0.111)	(-0.002, -0.028)	(0.721, 0.759)

TABLE VII: Same as in Table III but for $B^+ \rightarrow D_{s1}\mu^+\nu$. The differential branching ratios are given in order of 10^{-4} GeV^{-2} .

[$-30.3^\circ, -24.9^\circ$]							
$q^2 = \text{GeV}^2$	$\langle d\mathcal{B}/dq^2 \rangle$	$\langle d\mathcal{B}_L/dq^2 \rangle$	$\langle d\mathcal{B}_T/dq^2 \rangle$	$\langle \hat{\mathcal{A}}_{\text{FB}} \rangle$	$\langle \hat{\mathcal{A}}_{\text{FBL}} \rangle$	$\langle \hat{\mathcal{A}}_{\text{FBT}} \rangle$	$\langle \hat{F}_L \rangle$
[0.01 – 1]	(1.036, 1.201)	(1.007, 1.163)	(0.028, 0.037)	(0.024, 0.028)	(0.038, 0.039)	(-0.011, -0.014)	(0.966, 0.970)
[1 – 2]	(0.866, 1.017)	(0.784, 0.909)	(0.082, 0.108)	(-0.034, -0.047)	(0.008, 0.009)	(-0.044, -0.056)	(0.922, 0.936)
[2 – 3]	(0.697, 0.833)	(0.575, 0.673)	(0.122, 0.160)	(-0.085, -0.109)	(0.005, 0.006)	(-0.091, -0.115)	(0.858, 0.879)
[3 – 4]	(0.551, 0.671)	(0.406, 0.481)	(0.145, 0.190)	(-0.145, -0.181)	(0.003, 0.004)	(-0.149, -0.185)	(0.787, 0.814)
[4 – 5]	(0.523, 0.551)	(0.272, 0.328)	(0.148, 0.194)	(-0.208, -0.253)	(0.002, 0.003)	(-0.211, -0.256)	(0.715, 0.744)
[5 – 6]	(0.304, 0.385)	(0.171, 0.210)	(0.133, 0.175)	(0.001, 0.002)	(-0.264, -0.313)	(-0.264, -0.313)	(0.646, 0.674)
[6 – 7]	(0.200, 0.259)	(0.096, 0.121)	(0.103, 0.137)	(-0.262, -0.311)	(0.001, 0.002)	(-0.291, -0.333)	(0.583, 0.607)
[7 – 8.11]	(0.086, 0.115)	(0.034, 0.045)	(0.051, 0.069)	(-0.214, -0.232)	($\sim 10^{-4}$)	(-0.214, -0.233)	0.521, 0.537
[$43.3^\circ, 49.9^\circ$]							
[0.01 – 1]	(0.526, 0.827)	(0.443, 0.734)	(0.083, 0.091)	(-0.028, -0.046)	(0.027, 0.031)	-0.056, -0.077	(0.886, 0.915)
[1 – 2]	(0.585, 0.849)	(0.355, 0.592)	(0.230, 0.257)	(-0.198, -0.245)	(0.004, 0.005)	(-0.204, -0.250)	(0.721, 0.789)
[2 – 3]	(0.640, 0.864)	(0.308, 0.492)	(0.322, 0.371)	(-0.357, -0.405)	(0.002, 0.003)	(-0.360, -0.407)	(0.604, 0.682)
[3 – 4]	(0.654, 0.839)	(0.266, 0.405)	(0.387, 0.434)	(-0.497, -0.532)	(0.001, 0.002)	(-0.498, -0.534)	(0.600, 0.604)
[4 – 5]	(0.624, 0.771)	(0.227, 0.326)	(0.396, 0.444)	(-0.584, -0.626)	($\sim 10^{-4}$)	(-0.585, -0.627)	(0.473, 0.539)
[5 – 6]	(0.551, 0.663)	(0.187, 0.254)	(0.364, 0.408)	(-0.611, -0.660)	($\sim 10^{-4}$)	(-0.612, -0.661)	(0.441, 0.495)
[6 – 7]	(0.441, 0.518)	(0.144, 0.185)	(0.296, 0.332)	(-0.556, -0.605)	($\sim 10^{-4}$)	(-0.556, -0.606)	(0.425, 0.467)
[7 – 8.11]	(0.227, 0.239)	(0.078, 0.094)	(0.161, 0.182)	(-0.311, -0.342)	($\sim 10^{-4}$)	(-0.311, -0.342)	(0.427, 0.454)

TABLE VIII: Same as in Table IV but for $B^+ \rightarrow D_{s1}\tau^+\nu$. The differential branching ratios are given in order of 10^{-5} GeV^{-2} .

[$-30.3^\circ, -24.9^\circ$]							
$q^2 = \text{GeV}^2$	$\langle d\mathcal{B}/dq^2 \rangle$	$\langle d\mathcal{B}_L/dq^2 \rangle$	$\langle d\mathcal{B}_T/dq^2 \rangle$	$\langle \hat{\mathcal{A}}_{\text{FB}} \rangle$	$\langle \hat{\mathcal{A}}_{\text{FBL}} \rangle$	$\langle \hat{\mathcal{A}}_{\text{FBT}} \rangle$	$\langle \hat{F}_L \rangle$
[3.13 – 4]	(0.203, 0.146)	(0.198, 0.329)	(0.005, 0.007)	(0.122, 0.125)	(0.127, 0.130)	(-0.004, -0.005)	(0.987, 0.988)
[4 – 5]	(0.834, 1.005)	(0.776, 0.930)	(0.057, 0.074)	(0.186, 0.196)	(0.212, 0.218)	(-0.022, -0.025)	(0.958, 0.962)
[5 – 6]	(1.005, 1.217)	(0.873, 1.044)	(0.132, 0.172)	(0.165, 0.181)	(0.223, 0.231)	(-0.050, -0.057)	(0.916, 0.924)
[6 – 7]	(0.781, 0.956)	(0.614, 0.737)	(0.166, 0.219)	(0.118, 0.140)	(0.217, 0.226)	(-0.085, -0.089)	(0.865, 0.877)
[7 – 8.45]	(0.315, 0.398)	(0.202, 0.247)	(0.112, 0.166)	(0.050, 0.073)	(0.200, 0.211)	(-0.111, -0.121)	(0.783, 0.800)
[$43.3^\circ, 49.9^\circ$]							
[3.13 – 4]	(0.244, 0.301)	(0.230, 0.285)	(0.014, 0.015)	(0.093, 0.098)	(0.104, 0.108)	(-0.010, -0.011)	(0.977, 0.979)
[4 – 5]	(1.007, 1.233)	(0.858, 1.067)	(0.149, 0.165)	(0.091, 0.102)	(0.151, 0.162)	(-0.058, -0.061)	(0.914, 0.923)
[5 – 6]	(1.310, 1.583)	(0.960, 1.192)	(0.350, 0.390)	(0.006, 0.019)	(0.141, 0.154)	(-0.133, -0.138)	(0.831, 0.847)
[6 – 7]	(1.183, 1.404)	(0.719, 0.885)	(0.464, 0.518)	(-0.070, -0.080)	(0.121, 0.134)	(-0.206, -0.211)	(0.742, 0.763)
[7 – 8.45]	(0.644, 0.748)	(0.434, 0.522)	(0.344, 0.388)	(-0.102, -0.110)	(0.084, 0.101)	(-0.184, -0.192)	(0.635, 0.656)

TABLE IX: Same as in Table III but for $B^+ \rightarrow D_{s1}^{\prime-} \mu^+ \nu$. The differential branching ratios are given in order of 10^{-4} GeV^{-2} .

[$-30.3^\circ, -24.9^\circ$]							
$q^2 = \text{GeV}^2$	$\langle d\mathcal{B}/dq^2 \rangle$	$\langle d\mathcal{B}_L/dq^2 \rangle$	$\langle d\mathcal{B}_T/dq^2 \rangle$	$\langle \hat{\mathcal{A}}_{\text{FB}} \rangle$	$\langle \hat{\mathcal{A}}_{\text{FBL}} \rangle$	$\langle \hat{\mathcal{A}}_{\text{FBT}} \rangle$	$\langle \hat{F}_L \rangle$
[0.01 – 1]	(0.195, 0.363)	(0.136, 0.294)	(0.058, 0.068)	(-0.062, -0.104)	(0.027, 0.028)	(-0.087, -0.131)	(0.794, 0.867)
[1 – 2]	(0.270, 0.429)	(0.111, 0.241)	(0.159, 0.188)	(-0.256, -0.323)	(0.003, 0.004)	(-0.259, -0.327)	(0.554, 0.685)
[2 – 3]	(0.334, 0.480)	(0.108, 0.213)	(0.159, 0.267)	(-0.394, -0.445)	(0.001, 0.002)	(-0.396, -0.446)	(0.444, 0.596)
[3 – 4]	(0.464, 0.494)	(0.105, 0.188)	(0.258, 0.306)	(-0.485, -0.530)	($\sim 10^{-4}$)	(-0.486, -0.531)	(0.391, 0.497)
[4 – 5]	(0.359, 0.470)	(0.100, 0.163)	(0.259, 0.307)	(-0.525, -0.578)	($\sim 10^{-4}$)	(-0.525, -0.579)	(0.367, 0.453)
[5 – 6]	(0.322, 0.409)	(0.091, 0.135)	(0.231, 0.274)	(-0.510, -0.567)	($\sim 10^{-4}$)	(-0.510, -0.568)	(0.362, 0.428)
[6 – 7]	(0.253, 0.314)	(0.091, 0.102)	(0.178, 0.212)	(-0.422, -0.474)	($\sim 10^{-4}$)	(-0.423, -0.475)	(0.371, 0.420)
[7 – 8.41]	(0.137, 0.168)	(0.043, 0.055)	(0.094, 0.113)	(-0.220, -0.248)	($\sim 10^{-4}$)	(-0.220, -0.249)	(0.390, 0.420)
[$43.3^\circ, 49.9^\circ$]							
[0.01 – 1]	(0.613, 0.762)	(0.606, 0.747)	(0.007, 0.014)	(0.032, 0.037)	(0.039, 0.041)	(-0.004, -0.007)	(0.975, 0.980)
[1 – 2]	(0.484, 0.615)	(0.642, 0.574)	(0.021, 0.041)	(-0.008, -0.018)	(0.009, 0.010)	(-0.018, -0.029)	(0.952, 0.968)
[2 – 3]	(0.353, 0.467)	(0.320, 0.405)	(0.033, 0.061)	(-0.033, -0.055)	(0.005, 0.006)	(-0.039, -0.061)	(0.905, 0.934)
[3 – 4]	(0.248, 0.344)	(0.208, 0.271)	(0.039, 0.072)	(-0.063, -0.098)	(0.004, 0.005)	(-0.068, -0.102)	(0.847, 0.887)
[4 – 5]	(0.165, 0.243)	(0.125, 0.170)	(0.039, 0.073)	(-0.101, -0.146)	(0.003, 0.004)	(-0.105, -0.149)	(0.779, 0.828)
[5 – 6]	(0.101, 0.159)	(0.067, 0.096)	(0.033, 0.063)	(-0.143, -0.192)	(0.002, 0.003)	(-0.146, -0.195)	(0.705, 0.757)
[6 – 7]	(0.053, 0.092)	(0.029, 0.046)	(0.023, 0.045)	(-0.177, -0.219)	(0.001, 0.002)	(-0.179, -0.221)	(0.628, 0.676)
[7 – 8.41]	(0.019, 0.036)	(0.008, 0.014)	(0.010, 0.021)	(-0.152, -0.168)	($\sim 10^{-4}$)	(-0.153, -0.169)	(0.570, 0.616)

TABLE X: Same as in Table IV but for $B^+ \rightarrow D_{s1}^{\prime-} \tau^+ \nu$. The differential branching ratios are given in order of 10^{-5} GeV^{-2} .

[$-30.3^\circ, -24.9^\circ$]							
$q^2 = \text{GeV}^2$	$\langle d\mathcal{B}/dq^2 \rangle$	$\langle d\mathcal{B}_L/dq^2 \rangle$	$\langle d\mathcal{B}_T/dq^2 \rangle$	$\langle \hat{\mathcal{A}}_{\text{FB}} \rangle$	$\langle \hat{\mathcal{A}}_{\text{FBL}} \rangle$	$\langle \hat{\mathcal{A}}_{\text{FBT}} \rangle$	$\langle \hat{F}_L \rangle$
[3.13 – 4]	(0.114, 0.153)	(0.105, 0.142)	(0.009, 0.010)	(0.081, 0.089)	(0.096, 0.103)	(-0.013, -0.015)	(0.970, 0.980)
[4 – 5]	(0.477, 0.630)	(0.381, 0.517)	(0.096, 0.112)	(0.055, 0.071)	(0.128, 0.143)	(-0.069, -0.074)	(0.881, 0.896)
[5 – 6]	(0.632, 0.814)	(0.413, 0.556)	(0.218, 0.257)	(-0.020, -0.040)	(0.107, 0.126)	(-0.146, -0.152)	(0.774, 0.798)
[6 – 7]	(0.569, 0.715)	(0.295, 0.413)	(0.273, 0.323)	(-0.106, -0.118)	(0.101, 0.107)	(-0.200, -0.209)	(0.669, 0.699)
[7 – 8.41]	(0.319, 0.392)	(0.129, 0.164)	(0.189, 0.227)	(-0.101, -0.109)	(0.047, 0.061)	(-0.153, -0.166)	(0.606, 0.630)
[$43.3^\circ, 49.9^\circ$]							
[3.13 – 4]	(0.075, 0.111)	(0.073, 0.108)	(0.001, 0.002)	(0.133, 0.142)	(0.137, 0.145)	(-0.002, -0.003)	(0.980, 0.990)
[4 – 5]	(0.309, 0.452)	(0.294, 0.424)	(0.015, 0.028)	(0.215, 0.236)	(0.234, 0.250)	(-0.014, -0.018)	(0.966, 0.973)
[5 – 6]	(0.352, 0.517)	(0.319, 0.455)	(0.033, 0.062)	(0.208, 0.236)	(0.249, 0.267)	(-0.030, -0.041)	(0.932, 0.947)
[6 – 7]	(0.234, 0.354)	(0.196, 0.282)	(0.037, 0.071)	(0.174, 0.210)	(0.245, 0.264)	(-0.054, -0.071)	(0.888, 0.914)
[7 – 8.41]	(0.076, 0.125)	(0.053, 0.080)	(0.022, 0.044)	(0.111, 0.152)	(0.204, 0.232)	(-0.078, -0.094)	(0.827, 0.866)

TABLE XI: Bin-wise values of the ratio $\mathcal{R}_{D_{(s)1}^{(\prime)}}(q^2)$ for the decay $B_{(s)}^{0,+} \rightarrow D_{(s)1}^{(\prime)}\tau^{+\nu}/B_{(s)}^{0,+} \rightarrow D_{(s)1}^{(\prime)}\mu^{+\nu}$ in different q^2 intervals.

[−30.3°, −24.9°]				
q^2 (GeV ²)	$\langle\mathcal{R}_{D_1}\rangle$	$\langle\mathcal{R}_{D'_1}\rangle$	$\langle\mathcal{R}_{D_{s1}}\rangle$	$\langle\mathcal{R}_{D'_{s1}}\rangle$
[3.13 – 4]	(0.021, 0.025)	(0.024, 0.025)	(0.044, 0.046)	(0.036, 0.037)
[4 – 5]	(0.122, 0.124)	(0.121, 0.123)	(0.195, 0.201)	(0.183, 0.189)
[5 – 6]	(0.192, 0.195)	(0.190, 0.193)	(0.318, 0.332)	(0.292, 0.306)
[6 – 7]	(0.222, 0.227)	(0.220, 0.224)	(0.370, 0.390)	(0.328, 0.346)
$[7 - (m_{B_{(s)}^{0,+}} - m_{D_{(s)1}^{(\prime)}})^2]$	(0.234, 0.241)	(0.225, 0.232)	(0.329, 0.343)	(0.287, 0.298)
[43.3°, 49.9°]				
[3.13 – 4]	(0.027, 0.031)	(0.026, 0.027)	(0.040, 0.044)	(0.32, 0.035)
[4 – 5]	(0.115, 0.120)	(0.114, 0.119)	(0.155, 0.167)	(0.142, 0.152)
[5 – 6]	(0.170, 0.176)	(0.168, 0.174)	(0.231, 0.246)	(0.210, 0.223)
[6 – 7]	(0.200, 0.205)	(0.216, 0.220)	(0.263, 0.276)	(0.237, 0.248)
$[7 - (m_{B_{(s)}^{0,+}} - m_{D_{(s)1}^{(\prime)}})^2]$	(0.220, 0.225)	(0.225, 0.232)	(0.263, 0.270)	(0.239, 0.244)

Appendix A: Decay Kinematics and Scalar Products for Unpolarized Final State meson

The relevant non zero scalar products among the four momenta of initial meson, final state meson, charge lepton and neutrino i.e., p^μ , k^μ , p_1^μ and p_2^μ respectively are defined as

$$p_1^\mu p_{1\mu} = m_\ell^2, \quad p_2^\mu p_{2\mu} = 0, \quad p^\mu p_\mu = m_{B_{(s)}^{0,+}}^2, \quad k^\mu k_\mu = m_{D_{(s)1}^{(\prime)}}^2, \quad q^\mu q_\mu = q^2, \quad p_1^\mu p_{2\mu} = \frac{q^2 - m_\ell^2}{2}. \quad (\text{A1})$$

The scalar product between the charged lepton with the final state meson is given by,

$$p^\mu k_\mu = \frac{m_{B_{(s)}^{0,+}}^2 + m_{D_{(s)1}^{(\prime)}}^2 - q^2}{2}, \quad k^\mu p_{1\mu} = \frac{(q^2 + m_\ell^2)(m_{B_{(s)}^{0,+}}^2 - m_{D_{(s)1}^{(\prime)}}^2 - q^2) - (q^2 - m_\ell^2)\sqrt{\lambda(m_{B_{(s)}^{0,+}}^2, m_{D_{(s)1}^{(\prime)}}^2, q^2)} \cos\theta}{4q^2}. \quad (\text{A2})$$

with the momentum transfer defined as $q^\mu = p^\mu - k^\mu$ along with $P^\mu = p^\mu + k^\mu$, the following scalar products then hold,

$$k^\mu q_\mu = k^\mu p_\mu - k^\mu k_\mu, \quad p^\mu q_\mu = p^\mu p_\mu - p^\mu k_\mu, \quad p_1^\mu q_\mu = p_1^\mu p_{1\mu} - k^\mu p_{1\mu}, \quad p_2^\mu q_\mu = p_2^\mu p_{2\mu} - k^\mu p_{2\mu}, \quad (\text{A3})$$

$$p^\mu p_{1\mu} = p_1^\mu p_{1\mu} + p_1^\mu p_{2\mu} + p_1^\mu k_\mu, \quad p^\mu p_{2\mu} = p_2^\mu p_{2\mu} - p_1^\mu p_{1\mu} - p_1^\mu k_\mu, \quad k^\mu p_{2\mu} = k^\mu p_\mu - k^\mu k_\mu - k^\mu p_{1\mu}. \quad (\text{A4})$$

Appendix B: Decay Kinematics and Scalar Products for Longitudinal polarized Final State meson

For the longitudinal polarized final state meson the non zero scalar products are given,

$$k \cdot \varepsilon^*(k) = k \cdot \varepsilon(k) = 0, \quad \varepsilon^*(k) \cdot \varepsilon(k) = -1, \quad (\text{B1})$$

$$p \cdot \varepsilon(k) = p \cdot \varepsilon^*(k) = q \cdot \varepsilon(k) = q \cdot \varepsilon^*(k) = \frac{\sqrt{\lambda(m_{B(s)}^{2,0,+}, m_{D(s)1}^{2(\prime)}, q^2)}}{2m_{D(s)1}^{2(\prime)}}, \quad (\text{B2})$$

$$p_1 \cdot \varepsilon(k) = p_1 \cdot \varepsilon^*(k) = \frac{1}{m_{D(s)1}^{2(\prime)}} \left(\frac{\sqrt{\lambda(m_{B(s)}^{2,0,+}, m_{D(s)1}^{2(\prime)}, q^2)}}{4} - \frac{1}{4} \sqrt{1 - \frac{m_\ell^2}{q^2}} (m_{B(s)}^{2,0,+} - m_{D(s)1}^{2(\prime)} - q^2) \cos \theta \right), \quad (\text{B3})$$

$$p_2 \cdot \varepsilon(k) = p_2 \cdot \varepsilon^*(k) = \frac{1}{m_{D(s)1}^{2(\prime)}} \left(\frac{\sqrt{\lambda(m_{B(s)}^{2,0,+}, m_{D(s)1}^{2(\prime)}, q^2)}}{4} + \frac{1}{4} \sqrt{1 - \frac{m_\ell^2}{q^2}} (m_{B(s)}^{2,0,+} - m_{D(s)1}^{2(\prime)} - q^2) \cos \theta \right). \quad (\text{B4})$$

Appendix C: Decay Kinematics and Scalar Products for Transverse polarized Final State meson

For the transverse polarized final state meson the non zero scalar products are given,

$$\varepsilon^*(k) \cdot \varepsilon(k) = -1, \quad \varepsilon_{\mu\nu\rho\sigma} k^\mu p^\nu \varepsilon^{*\rho}(k) \varepsilon^\sigma(k) = 0, \quad \varepsilon_{\mu\nu\rho\sigma} p_1^\mu p_2^\nu \varepsilon^{*\rho}(k) \varepsilon^\sigma(k) = 0, \quad (\text{C1})$$

$$p_1 \cdot \varepsilon(k) = p_1 \cdot \varepsilon^*(k) = -\frac{\sqrt{q^2 - m_\ell^2}}{2\sqrt{2}} \sqrt{1 - \cos^2 \theta}, \quad p_2 \cdot \varepsilon(k) = p_2 \cdot \varepsilon^*(k) = \frac{\sqrt{q^2 - m_\ell^2}}{2\sqrt{2}} \sqrt{1 - \cos^2 \theta}, \quad (\text{C2})$$

$$p \cdot \varepsilon(k) = p \cdot \varepsilon^*(k) = \frac{\sqrt{\lambda(m_{B(s)}^{2,0,+}, m_{D(s)1}^{2(\prime)}, q^2)}}{2m_{D(s)1}^{2(\prime)}}, \quad q \cdot \varepsilon(k) = q \cdot \varepsilon^*(k) = \frac{\sqrt{\lambda(m_{B(s)}^{2,0,+}, m_{D(s)1}^{2(\prime)}, q^2)}}{2m_{D(s)1}^{2(\prime)}}, \quad (\text{C3})$$

$$p_1 \cdot \varepsilon(k) = p_1 \cdot \varepsilon^*(k) = \frac{1}{m_{D(s)1}^{2(\prime)}} \left(\frac{\sqrt{\lambda(m_{B(s)}^{2,0,+}, m_{D(s)1}^{2(\prime)}, q^2)}}{4} - \frac{\sqrt{q^2 - m_\ell^2}}{4\sqrt{s}} (m_{B(s)}^{2,0,+} - m_{D(s)1}^{2(\prime)} - q^2) \cos \theta \right), \quad (\text{C4})$$

$$p_2 \cdot \varepsilon(k) = p_2 \cdot \varepsilon^*(k) = \frac{1}{m_{D(s)1}^{2(\prime)}} \left(\frac{\sqrt{\lambda(m_{B(s)}^{2,0,+}, m_{D(s)1}^{2(\prime)}, q^2)}}{4} + \frac{\sqrt{q^2 - m_\ell^2}}{4\sqrt{q^2}} (m_{B(s)}^{2,0,+} - m_{D(s)1}^{2(\prime)} - q^2) \cos \theta \right). \quad (\text{C5})$$

$$\varepsilon_{\mu\nu\rho\sigma} p_1^\mu k^\nu p^\rho \varepsilon^\sigma(k) = \varepsilon_{\mu\nu\rho\sigma} k^\mu p^\nu p_1^\rho \varepsilon^\sigma(k) = \varepsilon_{\mu\nu\rho\sigma} k^\mu p^\nu p_2^\rho \varepsilon^{*\sigma}(k) = -\frac{iG\sqrt{q^2 - m_\ell^2}}{4\sqrt{2}} \sqrt{\lambda(m_{B(s)}^{2,0,+}, m_{D(s)1}^{2(\prime)}, q^2)} \sqrt{1 - \cos^2 \theta}, \quad (\text{C6})$$

$$\varepsilon_{\mu\nu\rho\sigma} k^\mu p^\nu p_1^\rho \varepsilon^{*\sigma}(k) = \varepsilon_{\mu\nu\rho\sigma} p_2^\mu k^\nu p^\rho \varepsilon^\sigma(k) = \varepsilon_{\mu\nu\rho\sigma} k^\mu p^\nu p_2^\rho \varepsilon^\sigma(k) = \frac{iG\sqrt{q^2 - m_\ell^2}}{4\sqrt{2}} \sqrt{\lambda(m_{B(s)}^{2,0,+}, m_{D(s)1}^{2(\prime)}, q^2)} \sqrt{1 - \cos^2 \theta}. \quad (\text{C7})$$

The remaining scalar products are zero.

-
- [1] D. Becirevic, A. Le Yaouanc, L. Oliver, J.-C. Raynal, P. Roudeau, and J. Serrano, *Proposal to study $B_s \rightarrow \bar{D}_{sJ}$ transitions*, *Phys. Rev. D* **87** (2013), no. 5 054007, [[arXiv:1206.5869](#)].
- [2] K. Azizi, H. Sundu, and S. Sahin, *Semileptonic $B_s \rightarrow D_{s2}^*(2573)\ell\bar{\nu}_\ell$ transition in QCD*, *Eur. Phys. J. C* **75** (2015), no. 5 197, [[arXiv:1411.3100](#)].
- [3] N. Alomayrah, J. S. Alzahrani, and M. S. Al-Buriahi, *Study on the semileptonic transition of $B_s \rightarrow D_{s2}(2900)\ell\nu_\ell$ in QCD: Promising case for the standard model*, *Nucl. Phys. A* **1027** (2022) 122512.
- [4] T. Barakat, *The semi-leptonic $B_s \rightarrow D_{s2}\ell\nu_\ell$ transition to tensor meson of negative parity in the QCD sum rules approach*, *Nucl. Phys. B* **983** (2022) 115915.
- [5] C.-W. Hwang and Z.-T. Wei, *Covariant light-front approach for heavy quarkonium: decay constants, $P \rightarrow \gamma\gamma$ and $V \rightarrow P\gamma$* , *J. Phys. G* **34** (2007) 687–702, [[hep-ph/0609036](#)].
- [6] S.-c. Li, Y. Jiang, T.-h. Wang, Q. Li, Z.-h. Wang, and G.-L. Wang, *Semi-leptonic production of $D_{sJ}(3040)$ and $D_J(3000)$ in B_s and B decays*, *Mod. Phys. Lett. A* **32** (2016), no. 03 1750013, [[arXiv:1608.07145](#)].
- [7] L.-F. Gan, J.-R. Zhang, M.-Q. Huang, H.-B. Zhuo, Y.-Y. Ma, Q.-J. Zhu, J.-X. Liu, and G.-B. Zhang, *$D_{sJ}(2860)$ From The Semileptonic Decays Of B_s Mesons*, *Eur. Phys. J. C* **75** (2015), no. 5 232, [[arXiv:1412.7969](#)].
- [8] T. M. Aliev, K. Azizi, and A. Ozpineci, *QCD sum rules analysis of the $B(s) \rightarrow D_{sJ}(2460)\ell\nu$ decay*, in *1st International Conference on Hadron Physics*, 1, 2008. [arXiv:0801.0958](#).
- [9] S.-M. Zhao, X. Liu, and S.-J. Li, *Study on $B_s \rightarrow D_{sJ}(2317, 2460)\ell\bar{\nu}$ Semileptonic Decays in the CQM Model*, *Eur. Phys. J. C* **51** (2007) 601–606, [[hep-ph/0612008](#)].
- [10] W. Wei, P.-Z. Huang, and S.-L. Zhu, *Strong decays of $D_{sJ}(2317)$ and $D_{sJ}(2460)$* , *Phys. Rev. D* **73** (2006) 034004, [[hep-ph/0510039](#)].
- [11] F.-L. Wang, X.-L. Chen, D.-H. Lu, S.-L. Zhu, and W.-Z. Deng, *Decays of $D_{sJ}^*(2317)$ and $D_{sJ}(2460)$ Mesons in the Quark Model*, *HEPNP* **30** (2006) 1041–1047, [[hep-ph/0604090](#)].
- [12] Z.-H. Wang, Y. Zhang, T.-h. Wang, Y. Jiang, Q. Li, and G.-L. Wang, *The Strong Decays of P-wave Mixing Heavy-Light 1^+ States*, *Chin. Phys. C* **42** (2018), no. 12 123101, [[arXiv:1803.06822](#)].
- [13] Y.-Y. Yang, Z.-Q. Zhang, and H. Yang, *Semileptonic $B_{(s)}$ meson decays to $D_0^*(2300)$, $D_{s0}^*(2317)$, $D_{s1}(2460)$, $D_{s1}(2536)$, $D_1(2420)$, and $D_1(2430)$ within the covariant light-front approach*, *Phys. Rev. D* **111** (2025), no. 7 076006.
- [14] S. Godfrey and N. Isgur, *Mesons in a Relativized Quark Model with Chromodynamics*, *Phys. Rev. D* **32** (1985) 189–231.
- [15] S. Godfrey and R. Kokoski, *The Properties of p Wave Mesons with One Heavy Quark*, *Phys. Rev. D* **43** (1991) 1679–1687.
- [16] Belle Collaboration, K. Abe et al., *Study of $B \rightarrow D_0^{**}\pi^- (D_0^{**} \rightarrow D^{(*)+}\pi^-)$ decays*, *Phys. Rev. D* **69** (2004) 112002, [[hep-ex/0307021](#)].
- [17] BaBar Collaboration, B. Aubert et al., *Dalitz Plot Analysis of $B^- \rightarrow D^+\pi^-\pi^-$* , *Phys. Rev. D* **79** (2009) 112004, [[arXiv:0901.1291](#)].
- [18] I. I. Bigi, B. Blossier, A. Le Yaouanc, L. Oliver, O. Pene, J. C. Raynal, A. Oyanguren, and P. Roudeau, *Memorino on the ‘1/2 vs. 3/2 Puzzle’ in $\bar{B} \rightarrow \ell\bar{\nu}X_c$ – a Year Later and a Bit Wiser*, *Eur. Phys. J. C* **52** (2007) 975–985, [[arXiv:0708.1621](#)].
- [19] V. Morenas, A. Le Yaouanc, L. Oliver, O. Pene, and J. C. Raynal, *Quantitative predictions for B semileptonic decays into D, D* and the orbitally excited D** in quark models a la Bakamjian-Thomas*, *Phys. Rev. D* **56** (1997) 5668–5680, [[hep-ph/9706265](#)].
- [20] D. Scora and N. Isgur, *Semileptonic meson decays in the quark model: An update*, *Phys. Rev. D* **52** (1995) 2783–2812, [[hep-ph/9503486](#)].
- [21] P. Colangelo, F. De Fazio, and N. Paver, *Universal $\tau_{1/2}(y)$ Isgur–Wise function at the next-to-leading order in QCD sum rules*, *Phys. Rev. D* **58** (1998) 116005, [[hep-ph/9804377](#)].
- [22] F.-W. Zhang and Z.-X. Zhao, *Weak decays of singly heavy baryons: the 1/2 \rightarrow 3/2 case*, [[arXiv:2508.13648](#)].
- [23] Belle Collaboration, F. Meier et al., *First observation of $B \rightarrow \bar{D}_1(\rightarrow \bar{D}\pi^+\pi^-)\ell^+\nu_\ell$ and measurement of the $B \rightarrow \bar{D}^{(*)}\pi\ell^+\nu_\ell$ and $B \rightarrow \bar{D}^{(*)}\pi^+\pi^-\ell^+\nu_\ell$ branching fractions with hadronic tagging at Belle*, *Phys. Rev. D* **107** (2023), no. 9 092003, [[arXiv:2211.09833](#)].
- [24] T. Barnes, F. E. Close, and H. J. Lipkin, *Implications of a DK molecule at 2.32-GeV*, *Phys. Rev. D* **68** (2003) 054006, [[hep-ph/0305025](#)].

- [25] J. Hofmann and M. F. M. Lutz, *Open charm meson resonances with negative strangeness*, *Nucl. Phys. A* **733** (2004) 142–152, [[hep-ph/0308263](#)].
- [26] H.-Y. Cheng and W.-S. Hou, *B decays as spectroscopy for charmed four quark states*, *Phys. Lett. B* **566** (2003) 193–200, [[hep-ph/0305038](#)].
- [27] M. A. Nowak, M. Rho, and I. Zahed, *Chiral Doubling of Heavy-Light Hadrons: BaBar 2317 MeV/c² and CLEO 2463 MeV/c² Discoveries*, *Acta Phys. Polon. B* **35** (2004) 2377–2392, [[hep-ph/0307102](#)].
- [28] T. E. Browder, S. Pakvasa, and A. A. Petrov, *Comment on the new $D_s^{(*)+}\pi^0$ resonances*, *Phys. Lett. B* **578** (2004) 365–368, [[hep-ph/0307054](#)].
- [29] W. A. Bardeen, E. J. Eichten, and C. T. Hill, *Chiral Multiplets of Heavy - Light Mesons*, *Phys. Rev. D* **68** (2003) 054024, [[hep-ph/0305049](#)].
- [30] Y.-Q. Chen and X.-Q. Li, *A Comprehensive Four-Quark Interpretation of $D_s(2317)$, $D_s(2457)$ and $D_s(2632)$* , *Phys. Rev. Lett.* **93** (2004) 232001, [[hep-ph/0407062](#)].
- [31] H. Kim and Y. Oh, *$D_s(2317)$ as a four-quark state in QCD sum rules*, *Phys. Rev. D* **72** (2005) 074012, [[hep-ph/0508251](#)].
- [32] E. E. Kolomeitsev and M. F. M. Lutz, *On Heavy light meson resonances and chiral symmetry*, *Phys. Lett. B* **582** (2004) 39–48, [[hep-ph/0307133](#)].
- [33] L. Maiani, F. Piccinini, A. D. Polosa, and V. Riquer, *Diquark-antidiquarks with hidden or open charm and the nature of $X(3872)$* , *Phys. Rev. D* **71** (2005) 014028, [[hep-ph/0412098](#)].
- [34] F.-K. Guo, P.-N. Shen, H.-C. Chiang, R.-G. Ping, and B.-S. Zou, *Dynamically generated 0^+ heavy mesons in a heavy chiral unitary approach*, *Phys. Lett. B* **641** (2006) 278–285, [[hep-ph/0603072](#)].
- [35] Z.-G. Wang and S.-L. Wan, *$D_{s0}(2317)$ as a tetraquark state with QCD sum rules in the heavy quark limit*, *Nucl. Phys. A* **778** (2006) 22–29, [[hep-ph/0602080](#)].
- [36] J. Vijande, F. Fernandez, and A. Valcarce, *Open-charm meson spectroscopy*, *Phys. Rev. D* **73** (2006) 034002, [[hep-ph/0601143](#)]. [Erratum: *Phys.Rev.D* 74, 059903 (2006)].
- [37] Z.-X. Xie, G.-Q. Feng, and X.-H. Guo, *Analyzing $D_{s0}^*(2317)^+$ in the DK molecule picture in the Bethe–Salpeter approach*, *Phys. Rev. D* **81** (2010) 036014.
- [38] M. Cleven, H. W. Griebhammer, F.-K. Guo, C. Hanhart, and U.-G. Meißner, *Strong and radiative decays of the $D_{s0}^*(2317)$ and $D_{s1}(2460)$* , *Eur. Phys. J. A* **50** (2014) 149, [[arXiv:1405.2242](#)].
- [39] c.-J. Xiao, D.-Y. Chen, and Y.-L. Ma, *Radiative and pionic transitions from the $D_{s1}(2460)$ to the $D_{s0}^*(2317)$* , *Phys. Rev. D* **93** (2016), no. 9 094011, [[arXiv:1601.06399](#)].
- [40] W. Wang, Y.-L. Shen, and C.-D. Lu, *The study of $B_c^- \rightarrow X(3872)\pi^-(K^-)$ decays in the covariant light-front approach*, *Eur. Phys. J. C* **51** (2007) 841–847, [[arXiv:0704.2493](#)].
- [41] H.-Y. Cheng, C.-K. Chua, and C.-W. Hwang, *Covariant light front approach for s wave and p wave mesons: Its application to decay constants and form-factors*, *Phys. Rev. D* **69** (2004) 074025, [[hep-ph/0310359](#)].
- [42] Y.-Y. Yang, Z.-Q. Zhang, H. Yang, Z.-J. Sun, and M.-X. Xie, *Study of $B_{(s)}$ meson decays to $D_0^*(2300)$, $D_{s0}^*(2317)$, $D_{s1}(2460)$ and $D_{s1}(2536)$ within the covariant light-front approach*, *Phys. Rev. D* **110** (2024), no. 3 033006, [[arXiv:2405.00496](#)].
- [43] H.-Y. Cheng and C.-K. Chua, *Covariant Light-Front Approach for $B \rightarrow K^*\gamma$, $K_1\gamma$, $K_2^*\gamma$ Decays*, *Phys. Rev. D* **69** (2004) 094007, [[hep-ph/0401141](#)]. [Erratum: *Phys.Rev.D* 81, 059901 (2010)].
- [44] C.-D. Lu, W. Wang, and Z.-T. Wei, *Heavy-to-light form factors on the light cone*, *Phys. Rev. D* **76** (2007) 014013, [[hep-ph/0701265](#)].
- [45] Wuenqi, R.-H. Li, and Z.-X. Zhao, *Semileptonic and nonleptonic $\bar{B}_s \rightarrow D_{sJ}$ decays in covariant light-front approach*, *Eur. Phys. J. C* **85** (2025), no. 9 1023, [[arXiv:2504.15056](#)].
- [46] H.-Y. Cheng, *Hadronic B decays involving even parity charmed mesons*, *Phys. Rev. D* **68** (2003) 094005, [[hep-ph/0307168](#)].
- [47] Y.-b. Dai and M.-q. Huang, *Semileptonic B decays into excited charmed mesons from QCD sum rules*, *Phys. Rev. D* **59** (1999) 034018, [[hep-ph/9807461](#)].
- [48] M.-q. Huang and Y.-b. Dai, *Subleading Isgur–Wise form factors and $\mathcal{O}(1/m_Q)$ corrections to the semileptonic decays $B \rightarrow D_1\ell\bar{\nu}$ and $B \rightarrow D_2^*\ell\bar{\nu}$* , *Phys. Rev. D* **64** (2001) 014034, [[hep-ph/0102299](#)].
- [49] Y.-B. Zuo, H.-Y. Jin, J.-Y. Tian, J. Yi, H.-Y. Gong, and T.-T. Pan, *$B_{(s)} \rightarrow D_{(s)}^{**}$ form factors in HQEFT and model independent analysis of relevant semileptonic decays with NP effects*, *Chin. Phys. C* **47** (2023), no. 10 103104, [[arXiv:2307.08271](#)].

- [50] N. Gubernari, A. Khodjamirian, R. Mandal, and T. Mannel, $B \rightarrow D_1(2420)$ and $B \rightarrow D_1'(2430)$ form factors from QCD light-cone sum rules, *JHEP* **05** (2022) 029, [[arXiv:2203.08493](#)].
- [51] A. K. Leibovich, Z. Ligeti, I. W. Stewart, and M. B. Wise, Predictions for $B \rightarrow D_1(2420)\ell\bar{\nu}$ and $B \rightarrow D_2^*(2460)\ell\bar{\nu}$ at order $\Lambda_{QCD}/m_{c,b}$, *Phys. Rev. Lett.* **78** (1997) 3995–3998, [[hep-ph/9703213](#)].
- [52] A. K. Leibovich, Z. Ligeti, I. W. Stewart, and M. B. Wise, Semileptonic B decays to excited charmed mesons, *Phys. Rev. D* **57** (1998) 308–330, [[hep-ph/9705467](#)].
- [53] F. U. Bernlochner and Z. Ligeti, Semileptonic $B_{(s)}$ decays to excited charmed mesons with e, μ, τ and searching for new physics with $R(D^{**})$, *Phys. Rev. D* **95** (2017), no. 1 014022, [[arXiv:1606.09300](#)].
- [54] F. U. Bernlochner, Z. Ligeti, and S. Turczyk, New ways to search for right-handed currents, *Phys. Rev. D* **96** (2017) 091503.
- [55] M. Blanke, A. Crivellin, S. de Boer, T. Kitahara, M. Moscati, U. Nierste, and I. Nišandžić, Impact of polarization observables and $B_c \rightarrow \tau\nu$ on new physics explanations of the $b \rightarrow c\tau\nu$ anomaly, *Phys. Rev. D* **99** (2019), no. 7 075006, [[arXiv:1811.09603](#)].
- [56] M. Fedele, M. Blanke, A. Crivellin, S. Iguro, T. Kitahara, U. Nierste, and R. Watanabe, Impact of $\Lambda_b \rightarrow \Lambda_c\tau\nu$ measurement on new physics in $b \rightarrow c\ell\nu$ transitions, *Phys. Rev. D* **107** (2023), no. 5 055005, [[arXiv:2211.14172](#)].
- [57] T. Yasmeen, I. Ahmed, S. Shafaq, M. Arslan, and M. J. Aslam, Probing New Physics in Light of Recent Developments in $b \rightarrow c \ell \nu$ Transitions, *PTEP* **2024** (2024), no. 7 073B07, [[arXiv:2401.02334](#)].
- [58] R. Dutta and N. Rajeev, Signature of lepton flavor universality violation in $B_s \rightarrow D_s\tau\nu$ semileptonic decays, *Phys. Rev. D* **97** (2018), no. 9 095045, [[arXiv:1803.03038](#)].
- [59] X.-Q. Li, Y.-D. Yang, and X. Zhang, Revisiting the one leptoquark solution to the $R(D^{**})$ anomalies and its phenomenological implications, *JHEP* **08** (2016) 054, [[arXiv:1605.09308](#)].
- [60] Y. Sakaki, M. Tanaka, A. Tayduganov, and R. Watanabe, Testing leptoquark models in $\bar{B} \rightarrow D^{**}\tau\bar{\nu}$, *Phys. Rev. D* **88** (2013), no. 9 094012, [[arXiv:1309.0301](#)].
- [61] **Fermilab Lattice, MILC Collaboration**, J. A. Bailey et al., Update of $|V_{cb}|$ from the $\bar{B} \rightarrow D^*\ell\bar{\nu}$ form factor at zero recoil with three-flavor lattice QCD, *Phys. Rev. D* **89** (2014), no. 11 114504, [[arXiv:1403.0635](#)].
- [62] Z. Ligeti, M. Papucci, and D. J. Robinson, New Physics in the Visible Final States of $B \rightarrow D^{**}\tau\nu$, *JHEP* **01** (2017) 083, [[arXiv:1610.02045](#)].
- [63] **Belle Collaboration**, A. Abdesselam et al., Measurement of the D^{*-} polarization in the decay $B^0 \rightarrow D^{*-}\tau^+\nu_\tau$, in *10th International Workshop on the CKM Unitarity Triangle*, 3, 2019. [[arXiv:1903.03102](#)].
- [64] **Belle Collaboration**, A. Abdesselam et al., Measurement of $\mathcal{R}(D)$ and $\mathcal{R}(D^*)$ with a semileptonic tagging method, [[arXiv:1904.08794](#)].
- [65] **LHCb Collaboration**, R. Aaij et al., Measurement of the ratio of branching fractions $\mathcal{B}(B_c^+ \rightarrow J/\psi\tau^+\nu_\tau)/\mathcal{B}(B_c^+ \rightarrow J/\psi\mu^+\nu_\mu)$, *Phys. Rev. Lett.* **120** (2018), no. 12 121801, [[arXiv:1711.05623](#)].
- [66] S. Kamali, A. Rashed, and A. Datta, New physics in inclusive $B \rightarrow X_c\ell\bar{\nu}$ decay in light of $R(D^{**})$ measurements, *Phys. Rev. D* **97** (2018), no. 9 095034, [[arXiv:1801.08259](#)].
- [67] P. Colangelo and F. De Fazio, Tension in the inclusive versus exclusive determinations of $|V_{cb}|$: a possible role of new physics, *Phys. Rev. D* **95** (2017), no. 1 011701, [[arXiv:1611.07387](#)].
- [68] Q. Chang, J. Zhu, N. Wang, and R.-M. Wang, Probing the effects of new physics in $\bar{B}^* \rightarrow P\ell\bar{\nu}_\ell$ decays, *Adv. High Energy Phys.* **2018** (2018) 7231354, [[arXiv:1808.02188](#)].
- [69] S. Mahata, M. Mandal, H. Mahapatra, S. Biswas, and S. Sahoo, Model dependent analysis of $D_{(s)}^+ \rightarrow \eta^{(\prime)}\ell^+\nu_\ell$ decays in beyond standard model, *Chin. Phys. C* **48** (2024), no. 9 093106, [[arXiv:2405.18254](#)].
- [70] S. Mahata, M. Mandal, S. Biswas, A. Biswas, and S. Sahoo, Investigation of $B_{d(s)}^* \rightarrow D_d^+(D_s^+)\tau^-\bar{\nu}_\tau$ decays in W' model and scalar leptoquark model, *Int. J. Mod. Phys. A* **38** (2023), no. 22n23 2350113.
- [71] K. Wei et al., Dark matter search with a resonantly-coupled hybrid spin system, *Rept. Prog. Phys.* **88** (2025), no. 5 057801, [[arXiv:2306.08039](#)].
- [72] S. Karmakar, S. Chattopadhyay, and A. Dighe, Identifying physics beyond SMEFT in the angular distribution of $\Lambda_b \rightarrow \Lambda_c(\rightarrow \Lambda\pi)\tau\bar{\nu}_\tau$ decay, *Phys. Rev. D* **110** (2024), no. 1 015010, [[arXiv:2305.16007](#)].
- [73] J.-H. Sheng, Q.-Y. Hu, R.-M. Wang, and J. Zhu, Phenomenology analysis of $\bar{B}^* \rightarrow V\tau^-\bar{\nu}_\tau$ decays in and beyond the Standard Model, *Eur. Phys. J. C* **82** (2022), no. 8 768.
- [74] J.-H. Sheng, J. Zhu, and Q.-Y. Hu, Investigation on the New Physics effects of the vector leptoquark on semileptonic $\bar{B}^* \rightarrow V\tau^-\bar{\nu}_\tau$ decays, *Eur. Phys. J. C* **81** (2021), no. 6 524.
- [75] J. Zhang, Y. Zhang, Q. Zeng, and R. Sun, New physics effects of the vector leptoquark on $\bar{B}^* \rightarrow P\tau\bar{\nu}_\tau$ decays, *Eur. Phys. J. C* **79** (2019), no. 2 164. [Erratum: *Eur.Phys.J.C* 79, 423 (2019)].

- [76] Z.-R. Huang, F. M. Bhutta, N. Farooq, M. A. Paracha, and Y. Li, *Reinvestigating the semileptonic $B \rightarrow D^{(*)}\tau\bar{\nu}_\tau$ decays in the model independent scenarios and leptoquark models*, *Phys. Rev. D* **111** (2025), no. 11 115035, [[arXiv:2501.03734](#)].
- [77] S. Zafar, Q. M. U. Salam, R. Khan, I. Ahmed, and R. Khalid, *Chirality structure of vector like new physics operators in charged current transitions*, *Eur. Phys. J. Plus* **140** (2025), no. 12 1167, [[arXiv:2507.23721](#)].
- [78] **Particle Data Group** Collaboration, S. Navas et al., *Review of particle physics*, *Phys. Rev. D* **110** (2024), no. 3 030001.
- [79] D. Bigi and P. Gambino, *Revisiting $B \rightarrow D\ell\nu$* , *Phys. Rev. D* **94** (2016), no. 9 094008, [[arXiv:1606.08030](#)].
- [80] F. U. Bernlochner, Z. Ligeti, M. Papucci, and D. J. Robinson, *Combined analysis of semileptonic b decays to d and D^* : $r(D^{(*)})$, $|V_{cb}|$, and new physics*, *Phys. Rev. D* **95** (Jun, 2017) 115008.
- [81] S. Jaiswal, S. Nandi, and S. K. Patra, *Extraction of $|V_{cb}|$ from $B \rightarrow D^{(*)}\ell\nu_\ell$ and the Standard Model predictions of $R(D^{(*)})$* , *JHEP* **12** (2017) 060, [[arXiv:1707.09977](#)].
- [82] S. Jaiswal, S. Nandi, and S. K. Patra, *Updates on extraction of $|V_{cb}|$ and SM prediction of $R(D^*)$ in $B \rightarrow D^*\ell\nu_\ell$ decays*, *JHEP* **06** (2020) 165, [[arXiv:2002.05726](#)].
- [83] P. Gambino, M. Jung, and S. Schacht, *The vcb puzzle: An update*, *Physics Letters B* **795** (2019) 386–390.
- [84] J. P. Lees and others (BaBar Collaboration), *Evidence for an excess of $\bar{B} \rightarrow D^{(*)}\tau^-\bar{\nu}_\tau$ decays*, *Phys. Rev. Lett.* **109** (2012) 101802, [[arXiv:1205.5442](#)].
- [85] M. Huschle and others (Belle Collaboration), *Measurement of the branching ratio of $\bar{B} \rightarrow D^{(*)}\tau^-\bar{\nu}_\tau$ relative to $\bar{B} \rightarrow D^{(*)}\ell^-\bar{\nu}_\ell$ decays with hadronic tagging at Belle*, *Phys. Rev. D* **92** (2015) 072014, [[arXiv:1507.03233](#)].
- [86] R. Aaij and others (LHCb Collaboration), *Measurement of the ratio of branching fractions $\mathcal{B}(\bar{B}^0 \rightarrow D^{*+}\tau^-\bar{\nu}_\tau)/\mathcal{B}(\bar{B}^0 \rightarrow D^{*+}\mu^-\bar{\nu}_\mu)$* , *Phys. Rev. Lett.* **115** (2015) 111803, [[arXiv:1506.08614](#)].
- [87] S. Fajfer, J. F. Kamenik, and I. Nisandzic, *On the $B \rightarrow D^*\tau\nu$ sensitivity to new physics*, *Phys. Rev. D* **85** (2012) 094025, [[arXiv:1203.2654](#)].